# Spin-dependent two-electron emission from ferromagnetic Fe(001)

F. Giebels,[1] H. Gollisch,[1] R. Feder,[1] F. O. Schumann,[2] C. Winkler,[2] and J. Kirschner[2]
[1]*Theoretische Festkörperphysik, Universität Duisburg-Essen, D-47048 Duisburg, Germany*
[2]*Max-Planck Institut für Mikrostrukturphysik, Weinberg 2, D-06120 Halle, Germany*
(Received 27 April 2011; published 11 October 2011)

We present a joint experimental and theoretical study of correlated electron pair emission from a ferromagnetic Fe(001) surface induced by spin-polarized low-energy electrons. Spin-dependent angular and energy distributions of the emitted pairs have been measured and calculated. They are analyzed with the aid of the spin-, momentum-, symmetry-, and layer-resolved valence electron density of states, which we obtained by an *ab initio* density-functional theory calculation. The observed spectra are found to arise almost completely from only three surface-parallel atomic layers. Momentum distributions for parallel spins of the emitted electrons exhibit an exchange-correlation hole, which is larger than the correlation hole in the antiparallel spin case. By comparing experimental antiparallel-spin pair spectra with their theoretical counterparts we determine an effective screening strength of the Coulomb interaction in the surface region.

DOI: 10.1103/PhysRevB.84.165421 PACS number(s): 73.20.At, 79.60.−i

## I. INTRODUCTION

Exchange and Coulomb correlation are of fundamental importance in many-electron systems like atoms, molecules, and solids. Experimentally, they are accessible by "correlation spectroscopy" alias "two-electron emission spectroscopy" techniques involving the momentum-resolved detection of pairs of time-correlated electrons, which emerge from the system following the collision of an incoming electron with a bound electron or the absorption of a single photon. According to whether the primary particle is an electron or a photon, the technique is commonly referred to as $(e,2e)$ or $(\gamma,2e)$ spectroscopy. Both techniques have a long history of intense experimental and theoretical study in atomic physics (cf., e.g., Refs. 1–3 and ample references therein).

For solid surface systems, two-electron emission spectroscopy has, both experimentally and theoretically, matured over the past decade. For $(e,2e)$, cf. the review article,[4] more recent papers,[5–11] and further references therein. For $(\gamma,2e)$, cf. the review article,[12] recent papers,[10,13,14] and references therein.

As a consequence of exchange and correlation, the reaction cross section has a minimum if the two electrons have the same energy and are emitted in the same direction. Around this minimum, the angular distribution exhibits a region of reduced pair emission intensity. This depletion zone constitutes an exchange-correlation hole in momentum space, in correspondence to the exchange-correlation hole in real space, which has been a central concept in the theory of many-electron systems since the early days of quantum mechanics[15,16] up to the present, in particular in the context of density-functional theory (cf., e.g., reviews[17–19] and ample references therein).

Such an exchange-correlation hole in momentum space has been intensely studied in $(\gamma,2e)$ for atoms (cf., e.g., Refs. 2 and 3, and references therein). For solid surfaces, it has first been identified theoretically in $(e,2e)$ calculations from W(001),[20] and experimentally in $(e,2e)$ from LiF.[5,8] Likewise, it was found and investigated in detail by $(\gamma,2e)$ (cf. Refs. 13 and 14, and references therein.

Both in $(e,2e)$ and in $(\gamma,2e)$ the observable exchange-correlation hole owes its very existence to exchange and Coulomb correlation in the two-electron final state. Its detailed shape is determined by Coulomb matrix elements in the case of $(e,2e)$ and by electric dipole matrix elements in the case of $(\gamma,2e)$. The latter entail a dependence of the hole on the polarization of the incident light, as was, e.g., found in a $(\gamma,2e)$ experiment for the Cu(111) surface.[14] The initial state, which enters in the matrix elements, is for $(e,2e)$ simply an antisymmetrized product of one-electron states, whereas for $(\gamma,2e)$ it is in general a Coulomb-correlated two-electron state, which makes a quantitative theoretical treatment more complicated.

If the spins of the two electrons are parallel, the hole in an angular distribution of the two outgoing electrons is produced by exchange (Pauli principle) and Coulomb interaction, whereas in the antiparallel-spin case it is due to only the Coulomb interaction. Controlling the relative spin orientation of the two electrons is easy in theory. Experimentally, one might, for both $(e,2e)$ and $(\gamma,2e)$, think of analyzing the spins of the two outgoing electrons. This is, however, presently not yet feasible. For $(e,2e)$, a viable alternative consists in using spin-polarized primary electrons and a ferromagnetic target.

Initial work on spin-dependent $(e,2e)$ from a ferromagnetic surface was carried out for fixed large emission angles.[21,22] Pair emission angular distributions over a wide range of emission angles were reported only very recently,[11] providing first experimental evidence for the spin dependence of the above-mentioned exchange-correlation hole in momentum space. In agreement with corresponding calculations, the central depletion zone in angular distributions was found to be more extended for parallel spins of the two electrons than for antiparallel spins.

In this paper, we present an in-depth experimental and theoretical study of spin-dependent $(e,2e)$ from the ferromagnetic Fe(001) surface. The focus is first on angular distributions (surface-parallel momentum distributions) for equal energies, and second on energy distributions (sharing curves) for a wide range of emission angles.

 

The theoretical part of this work, consisting of an *ab initio* ground-state calculation and realistic $(e,2e)$ intensity calculations, has four main aims. First, to explore how the spin-, $k_{||}$-, symmetry-, and layer-resolved valence electron density of states manifests itself in $(e,2e)$ energy and momentum distributions. Second, to identify valence electron energies and parallel momenta, for which either majority or minority spin strongly dominates, which provides an internal spin resolution for $(e,2e)$. Third, to reach a quantitative assessment of the high surface sensitivity of $(e,2e)$. Fourth, to determine, by comparing experimental and theoretical $(e,2e)$ spectra, an effective range of the screened Coulomb interaction in the surface region.

This paper is organized as follows. Section II is devoted to experimental details. We describe the apparatus used and the presentation of the measured $(e,2e)$ data in the form of spin-dependent energy and momentum distributions. In Sec. III we first outline our theoretical formalism and second present numerical results: fully resolved densities of states of Fe(001) together with fully spin-resolved $(e,2e)$ energy and momentum distributions. In Sec. IV we compare experimental and theoretical energy sharing curves and momentum distributions.

## II. EXPERIMENT

For the experimental study we built a time-of-flight (TOF) coincidence apparatus, which we described in more detail previously.[8] We have upgraded this setup with the implementation of a spin-polarized primary electron beam in a similar fashion as reported earlier.[21,22] The generation of spin-polarized electron beams is an established technique by now.[23] The key idea is to excite a GaAs surface with circular polarized light with a wavelength of about 800 nm. The treatment of the surface with Cs and $O_2$ lowers the work function sufficiently such that photoemission is possible with the low photon energy. The emitted electrons carry a longitudinal spin polarization that can be reversed by changing the helicity of the light. The longitudinal spin polarization is changed to a transversal spin polarization by means of an electrostatic 90° deflector.[21–23] The spin polarization was 40%. This spin-polarized electron beam hits the sample; we employed a geometry of normal incidence. The pulsing of the primary beam is achieved by using a fast laser diode as light source. The repetition rate was 2 MHz and the overall time resolution of the experiment is 1 ns. This uncertainty amounts to an energy resolution of 0.4 eV for 10-eV electrons. The primary beam has an energy spread of 100 meV. The emitted electrons are registered by two channel-plate detectors, which we label "left" and "right," respectively. These detectors are equipped with delay line anodes, which allow us to determine the impact position on the detector. With this knowledge we can determine the actual flight path taken and the emission angles with respect to the surface. The flight time can then be converted in kinetic energy, which finally allows us to compute the in-plane momentum. A coincidence circuit ensures that only one electron pair per incident electron pulse can be detected. In the following we will quote all kinetic energies with respect to the vacuum level. We have defined a coordinate system such that the $x$ and $y$ axis are in the surface plane; see Fig. 1. We have grown approximately 20-monolayer (ML)-thick Fe films on either a W(001) surface or MgO/W(001) surface. In this thickness range structure and electronic properties are bulklike except for the first few layers. The samples are magnetized in plane with the easy axis along the [010] direction, which is parallel to the $y$ axis, see Fig. 1. We can apply a pulsed magnetic field along the $y$ axis for reversing the magnetization. The spin polarization of the incoming beam is also along the $y$ axis. The primary spin polarization and majority spin direction can be individually controlled. Therefore the observed spectra can be grouped into two subsets: (i) for subset $I^+$ primary spin and majority spin directions are parallel, (ii) events with antiparallel alignment of primary electron and majority spin are contained in subset $I^-$. As it is customary in spin-polarized spectroscopy, the change of the relative spin orientation occurs frequently (every few minutes). This ensures that both spectra are obtained under identical conditions. The data acquisition times for both spin alignments are equal allowing direct comparison of the intensity levels. Typical acquisition times for a particular primary energy are a few weeks. The coincidence intensity was about 20 counts per second due to the requirement to operate at a low primary flux. The singles count rate was in the range 1000–2000 cps. Each coincident event is characterized by six coordinates, which are the individual kinetic energies and the two components of the in-plane momentum of each electron.

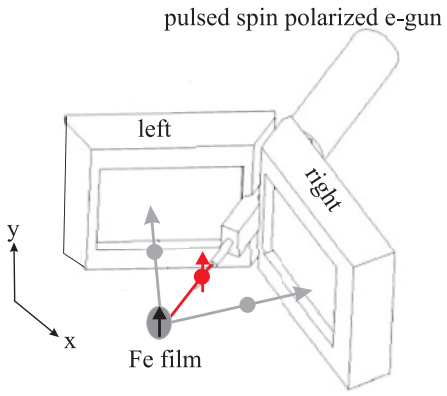


FIG. 1. (Color) Schematic view of the experiment. A transversely spin-polarized electron hits a ferromagnetic sample. The relative orientation of the majority and polarization direction can be independently reversed. Momentum distributions are obtained via position sensitive detectors and time-of-flight analysis.

### A. Momentum Presentations

We would like to move on and define some parameters that we will use later. If a primary electron hits a surface and a subsequent emission of an electron pair occurs energy conservation has to hold. In this context it is useful to define the sum energy of the pair $E_{\mathrm{sum}}$ as $E_{\mathrm{sum}} = E_l + E_r$ (energy of the left and right electron, respectively). If the valence electron has a binding energy $E_b$ we can write

$$E_{\mathrm{sum}} = E_l + E_r = E_p - \phi - E_b. \quad (1)$$

The sum energy of the pair is uniquely defined by the energy of the primary beam $E_p$, the work function $\phi$ of the specimen and the binding energy of the valence electron relative to $E_F$. Further we note that the maximum value $E_{\text{sum}}^{\text{max}}$ the sum energy can adopt is

$$E_{\text{sum}}^{\text{max}} = E_p - \phi. \tag{2}$$

This value is attained if the valence electron originates from the Fermi level $E_F$. We may rearrange Eq. (1) and find

$$E_b = E_p - \phi - E_{\text{sum}}. \tag{3}$$

This rearrangement highlights the fact that in contrast to theory we cannot select the valence state of the valence electron before the scattering. However, the value of $E_{\text{sum}}$ clearly identifies $E_b$.

Our target is a single crystalline surface therefore the in-plane component of the momentum must be conserved (modulo a reciprocal surface lattice vector). This can be written as

$$\mathbf{k}_\parallel^v + \mathbf{k}_\parallel^p = \mathbf{k}_\parallel^l + \mathbf{k}_\parallel^r = \mathbf{k}_\parallel^{\text{sum}}. \tag{4}$$

On the left side of the equation we have the contribution of the valence electron $\mathbf{k}_\parallel^v$ and the primary electron $\mathbf{k}_\parallel^p$, while on the right side the contribution of the detected electrons $\mathbf{k}_\parallel^l$ (left) and $\mathbf{k}_\parallel^r$ (right) can be found. The sum of these two terms is called sum momentum $\mathbf{k}_\parallel^{\text{sum}}$. Since we operate with a normal incidence primary beam we have $\mathbf{k}_\parallel^p = 0$. In this case Eq. (4) simplifies to

$$\mathbf{k}_\parallel^v = \mathbf{k}_\parallel^{\text{sum}}. \tag{5}$$

We note that $\mathbf{k}_\parallel^{\text{sum}}$ determines the value of the valence electron $\mathbf{k}_\parallel^v$. From Eqs. (3) and (5) and we learn that the momentum and the kinetic energies of the pair determine the momentum and binding energy of the valence electron. With an appropriate choice one has the freedom to focus on scattering events involving a particular valence state.

We would like to explain a bit more in detail how we obtain from our six-dimensional data set two-dimensional (2D)-momentum distributions. In a first step we determine the energy level of the valence state via the energies of the two outgoing electrons. For example, we studied the pair emission from a sample excited with a primary beam of 19 eV. The 2D-energy distribution from this experiment is plotted in Fig. 2. For this we have spin-integrated the data and include all emission directions captured by the detectors. From Eq. (2) we know that the highest value for $E_{\text{sum}}$ is attained if the valence electron originates from the Fermi level $E_F$. The work function for a Fe(001) surface is 4.7 eV, which together with the primary energy of 19 eV results in $E_{\text{sum}}^{\text{max}} = 14.3$ eV. This energy position has been marked by a dashed diagonal line in Fig. 2. We can clearly observe that the onset of pair emission occurs at this line, as expected. The small intensity above this line cannot be due to the emission of an electron pair following the impact of one primary electron; see Eq. (2). The intensity above $E_{\text{sum}}^{\text{max}}$ must be due to the impact of two primary electrons. These events we may call "random" coincidences in contrast to "true" coincidences, which are due to the impact of one primary electron. "Random" coincidences can also occur in the energy range where we expect true coincidences. We can estimate the intensity level in this region from the

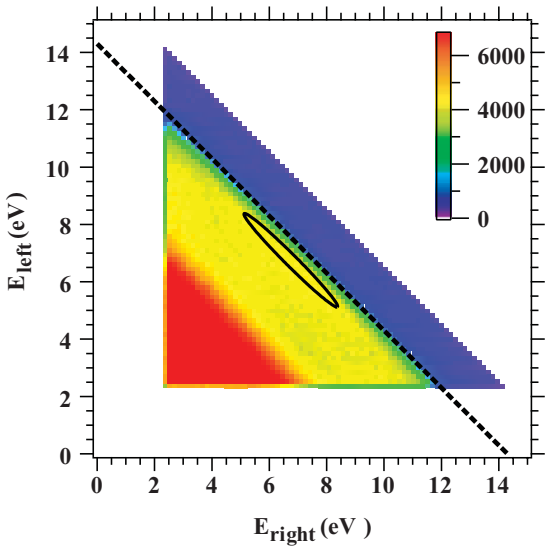


FIG. 2. (Color) 2D energy distribution from an experiment obtained with $E_p = 19$ eV. The dashed diagonal line marks the maximum energy $E_{\text{sum}}^{\text{max}} = 14.3$ eV that the pair can have. The ellipse marks the energy window selected for 2D-momentum presentations shown in Fig. 3.

intensity above $E_{\text{sum}}^{\text{max}}$. From this we can conclude that random coincidences do not play a major role. We also observe that a high portion of the coincidences are confined to the low-energy region of the spectrum. This is a general observation we made for different metals and insulators.

From simple energy considerations it is clear that events in this energy region must involve electrons that encountered inelastic scattering. In order to simplify the picture we will remove these events in further presentations. Out of the complete data set we select those that fulfill a certain energy constraint. For example, if the two emitted electrons have an energy of 6.75 eV, we obtain a sum energy of 13.5 eV. In order to have a sufficient statistics for a meaningful plot we allow electrons within a narrow energy window. This window is indicated by an ellipse in Fig. 2 and has a half axis of 2.25 and 0.3 eV, respectively. A sum energy of 13.5 eV leads via Eq. (3) to a binding energy of 0.8 eV below $E_F$ for the valence state involved in the scattering event. For this subset of the data we can compute a 2D-momentum distribution; see Fig. 3(a). We note that for each coincident event the in-plane components of electron left and right are known. According to our coordinate system $k_x^l$ is always negative while $k_x^r$ is positive. Therefore a coincidence event has an entry on the left and right half of the plot. In this plot we can immediately recognize the left and right detector, respectively. The white areas are regions in momentum space that are not covered by the detectors. We have included in Fig. 3(a) a circle centered at the origin of the coordinate system, which has a radius of 0.2 Å$^{-1}$. In order to select the momentum of the valence electron we have to put a constraint on the sum momentum; see Eq. (5). If we were to set $\mathbf{k}_\parallel^{\text{sum}} = 0$ the valence electron would come from the $\overline{\Gamma}$ point. In order to have sufficient statistics the experimental constraint has to be lowered and we usually take $|\mathbf{k}_\parallel^{\text{sum}}| \leqslant 0.2$ Å$^{-1}$. We emphasize that this is not due to an insufficient angular resolution of the experiment. The momentum distribution that

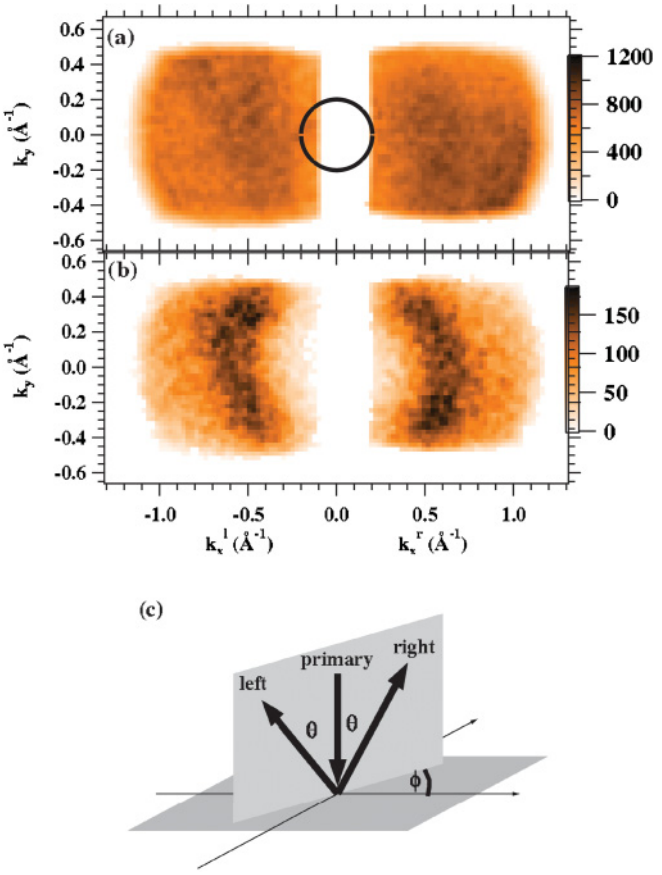


FIG. 3. (Color) Panels (a) and (b) display 2D-momentum presentations. These are obtained with a primary energy of 19 eV while the energies of the emitted electrons are $E_l = E_r = 6.75$ eV. This energy selection means that the valence electron comes from a state 0.8 eV below $E_F$. In (a) we display the spin-integrated intensity as a function of the in-plane momentum of electron left and right. The momentum distribution in (b) is obtained if the constraint $|\mathbf{k}_\parallel^{\rm sum}| \leqslant 0.2$ Å$^{-1}$ is imposed. This is fulfilled if $\mathbf{k}_\parallel^{\rm sum}$ falls within the circle.

results from this momentum constraint is plotted in Fig. 3(b). We see clearly that this momentum distribution is very different compared the more or less uniform distribution shown in Fig. 3(a). The selection of equal energies and $\mathbf{k}_\parallel^{\rm sum} = 0$ can also be visualized in a simple geometric fashion as depicted in panel (c). Coming back to panel (b) we see that starting at $|k_x^{l,r}| = 0$ the coincidence intensity is zero. This is purely instrumental since there is a gap between the detectors. Outside this "blind" region, starting at about $|k_x^{l,r}| = 0.2$ Å$^{-1}$, we observe an increase of the coincidence intensity for increasing $k$ values. A maximum is reached at $|k_x^{l,r}| \approx 0.5$ Å$^{-1}$. This reduced intensity for small $|k_x^{l,r}|$ values is a manifestation of the $xc$ hole as shown previously in experiment and theory.[5,7,24,25] We may call this region of reduced intensity depletion zone. Upon further increase of $|k_x^{l,r}|$ the coincidence decreases again. The drop to zero intensity on the very left and right of the plot is due to the finite angular acceptance of the detectors. At this point it is worth mentioning that in the previous experimental presentations of the depletion zone the emission direction of one electron was fixed while the emission direction of the other electron was varied. The kinetic energies had also definite values. In such a presentation valence states with different momentum will be probed as can be readily deduced from Eq. (4). In the following we will adopt the procedure by which we obtain momentum distributions from selected valence states. The imposed energy and momentum constraints have a similar window as the above described example. More precisely, we will focus on those valence states that are at the $\overline{\Gamma}$ point. Spin-dependent distributions can be computed if we take the subsets $I^+$ and $I^-$ separately. For a direct comparison of the momentum distributions from electrons of different kinetic energy it is useful to plot the data as a function of the normalized in-plane momentum. The selection to focus on events for which $\mathbf{k}_\parallel^{\rm sum} = 0$ can also be motivated in the following manner. For this we replot the data presented in Fig. 3 in two ways. Rather than using the individual momenta we compute for each event the value of the sum momentum $\mathbf{k}_\parallel^{\rm sum}$. This leads to a 2D-$k^{\rm sum}$ distribution, displayed in Fig. 4(a). The data exhibit a broad maximum centered at $\mathbf{k}_\parallel^{\rm sum} = 0$ and the circle added to panel (a) is identical to the one seen in Fig. 3(a). The size of this ring is solely determined by the need to include sufficient events for statistics. Clearly the best choice for a given ring diameter is to set $\mathbf{k}_\parallel^{\rm sum} = 0$. According to Eq. (5) the 2D-$k^{\rm sum}$ distribution is directly related to the 2D-momentum distribution of the valence states. Only if available valence states with the correct momentum exist, in our example 0.8 eV below $E_F$, is a scattering event possible. For the two-particle problem it is known that the motion can be decomposed in a center-of-mass and relative motion. In the (in-plane) momentum space the appropriate coordinates are the sum momentum $\mathbf{k}_\parallel^{\rm sum}$ and difference momentum $\mathbf{k}_\parallel^{\rm diff} = \mathbf{k}_\parallel^r - \mathbf{k}_\parallel^l$. It is appealing to present the coincidence events in a 2D plot where the $x$ axis is the $x$ component of $\mathbf{k}_\parallel^{\rm diff}$ and the $y$ axis is the $x$ component of $\mathbf{k}_\parallel^{\rm sum}$. The result is depicted in Fig. 4(b). At first sight it may come as a surprise that the $x$ component of $\mathbf{k}_\parallel^{\rm diff}$ is only positive, because electrons are not distinguishable. Therefore we should expect also negative values. However, our detection scheme is not symmetrical in the sense that we call one electron right and the other left. We note that the coincidence intensity in Fig. 4(b) is confined in a square region. This is an immediate consequence of the kinematics and not an instrumental artefact. For an instrument which covers the full half space the square region would be larger, but still exists. Within the square region we observe a vertical intensity band, which is the counterpart of the almost circular intensity rim seen in Fig. 3(b). A fixed angular correlation between emitted electrons manifests itself in a fixed value of $k^{\rm diff}$. From Fig. 4(b) we learn that the choice of $\mathbf{k}_\parallel^{\rm sum}$ does not single out particular $k^{\rm diff}$ values. Due to the fact that the range of $k^{\rm diff}$ values is larger if $\mathbf{k}_\parallel^{\rm sum} = 0$ is selected we will use this constraint in the following.

### B. Spin-dependent momentum presentations

As a first example of spin-dependent momentum distributions we select data obtained with $E_p = 25$ eV. Furthermore, we choose the valence electron to come from a state 0.8 eV below the $E_F$. This particular choice will be explained in more depth later. Consequently we plot in Fig. 5(a) the 2D-momentum distribution for parallel alignment of primary

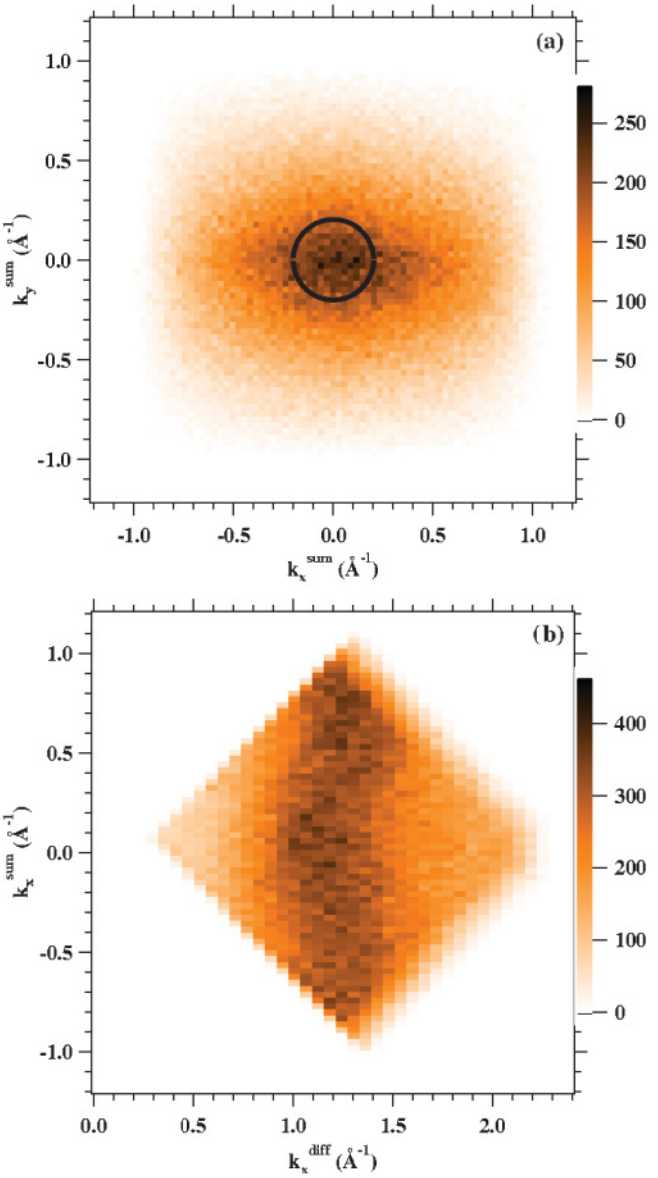


FIG. 4. (Color) 2D-momentum presentations obtained with a primary energy of 19 eV and energies of the emitted electrons $E_l = E_r = 6.75$ eV. This energy selection means that the valence electron comes from a state 0.8 eV below $E_F$. (a) Sum momentum $\mathbf{k}_\parallel^{\rm sum}$; (b) difference momentum $\mathbf{k}_\parallel^{\rm diff} = \mathbf{k}_\parallel^r - \mathbf{k}_\parallel^l$.

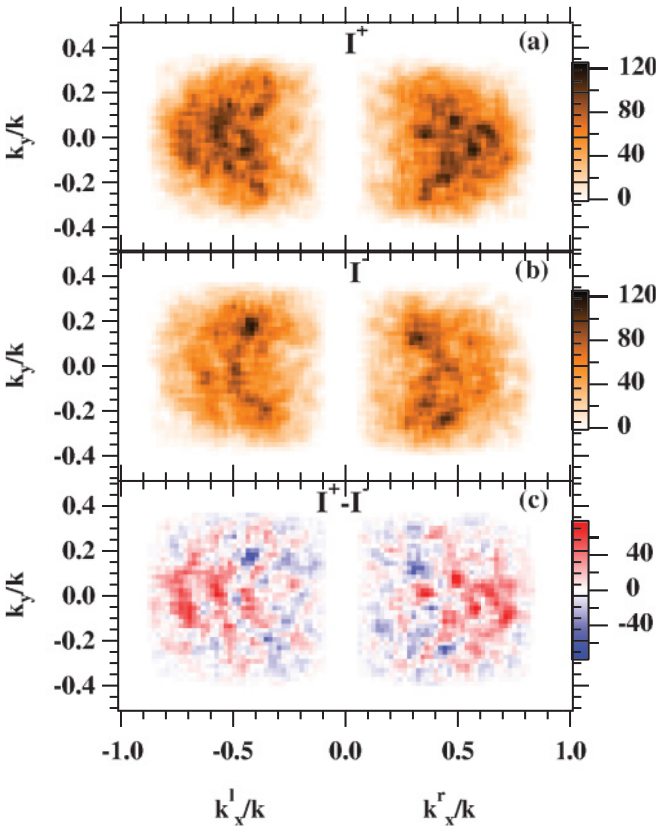


FIG. 5. (Color) Coincidence intensity versus normalized in-plane momentum. These are obtained with a primary energy of 25 eV while the energies of the emitted electrons are $E_l = E_r = 9.75$ eV. This energy selection means that the valence electron comes from a state 0.8 eV below $E_F$. In all panels we display the intensity as a function of the normalized in-plane momentum of electron left and right. In (a) we plot the intensity for subset $I^+$ (primary/majority spin parallel) while (b) shows the result for subset $I^-$ (primary/majority spin antiparallel). In (c) we display the difference spectrum $I^+$-$I^-$.

spin and majority spin (data set $I^+$). Panel (b) shows the equivalent distribution for antiparallel alignment of primary spin and majority spin (data set $I^-$). The color coding for panels (a) and (b) are identical therefore it is possible to directly compare the intensity levels. In order to highlight the differences between these two distributions we computed the difference spectrum $I^+$-$I^-$ in Fig. 5(c). As for the spin-integrated example presented in Fig. 3 we note that the intensity distributions display a region of reduced intensity if $|k_x^{l,r}/k| < 0.2$. After reaching the maximum intensity at $|k_x^{l,r}/k| \approx 0.5$ the intensity falls off for larger $|k_x^{l,r}/k|$ values. However, we note that the intensity for $I^+$ falls off less strongly compared to the $I^-$ case. The different intensity levels for $I^+$ and $I^-$ translate into a distribution of predominantly positive values indicated by larger areas of the color red. This intensity difference is strongest for $|k_x^{l,r}|$ values of about 0.8 Å$^{-1}$.

### C. Energy distributions

Another important aspect of the pair emission is the question of how the available energy between the two emitted electrons is shared. Having shown that the emission of pairs does show a momentum dependence or angular dependence for a given energy one may ask the inverse question. More precisely, what does the energy distribution look like if the emission angles are constrained? The presentation of the data in this way requires the execution of several steps. First we plot all coincidence events together and obtain what we call a hit pattern; see Fig. 6. This is essentially a sum of momentum distributions shown in Fig. 3(a). The main difference is that all energy combinations are allowed. Due to the fact that the momentum scales with the energy it is more appropriate to display the hit pattern as a function of the normalized components of the in-plane momentum. We note that the pattern is essentially uniform similar to the distribution plotted in Fig. 3(a). In a second step we select now those events that

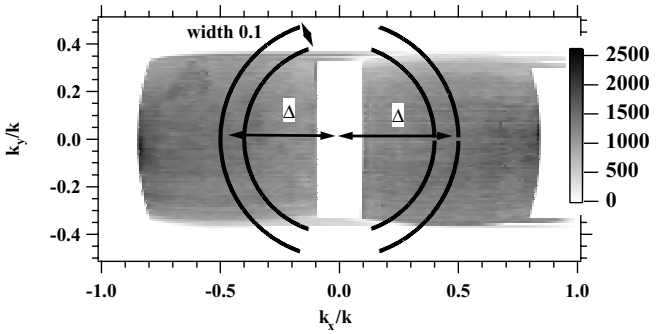


FIG. 6. The hit pattern of electron pairs is displayed. As axes we use the components of the normalized in-plane momentum of the individual electrons. The excitation was via a primary electron beam with 19 eV, which hit the sample along the surface normal. The pair of arcs on the left and right detectors define narrow regions that have a radius defined by Δ. We will select only those events where the left and right electrons come from those regions. The gray scale on the right displays the intensity in counts.

fulfill the following critereon. The electron that is registered on the left detector has to be within the region defined by the two arcs on the left. The counterpart of this electron has to be detected within the narrow region on the right detector. The mean radius of the pair of arcs has a value given by Δ when measured from the origin of the coordinate system. The separation of the arcs within one side is set to 0.10. This value is dictated by the statistics. A fixed value of Δ fixes the emission angle with respect to the surface normal regardless of the kinetic energy of the electrons. It is useful to point out that these constraints have a simple geometric meaning; see Fig. 3(c). We study those events for which the angle Θ with respect to the normal is fixed while the azimuthal angle $\phi$ for both electrons is a free parameter as long as the two electrons forming a pair leave the sample in opposite directions. We may proceed and display the spin-integrated 2D-energy distributions under such a geometrical constraint. In Fig. 7 we plot the energy distribution for three selected values of Δ. As stated above we have removed the low-energy portion because we want to focus on events that do not encounter inelastic scattering. In panel (a) we present the result for $\Delta = 0.2$. According to Fig. 3(c) this amounts to an emission angle $\Theta \approx 12^\circ$. We note that the pair emission has an onset at $E_{\text{sum}}^{\text{max}}$ where it becomes energetically possible for two electrons to leave the sample. The energetic position is marked by the solid diagonal line. However, we notice that this is only the case if the electron energies are rather unequal. As a matter of fact for all sum energies of the pair there is a preference for an electron to be "fast" while the other is "slow." This situation changes once we change to $\Delta = 0.5$ or $\Theta = 30^\circ$. Again we see the onset of pair emission where it is energetically possible to emit an electron pair. Further this is not confined to those events where the electrons have very unequal energies but is possible for all energy combinations. In all panels we have added another diagonal line, which is energetically 0.8 eV below $E_{\text{sum}}^{\text{max}}$. We observe an enhanced intensity for this value of $E_{\text{sum}}$ if the two electrons have equal energies. As a third example we set $\Delta = 0.7$ equivalent to $\Theta \approx 44^\circ$. Again we can see that the onset of the pair emission occurs at $E_{\text{sum}}^{\text{max}}$. Further, for a

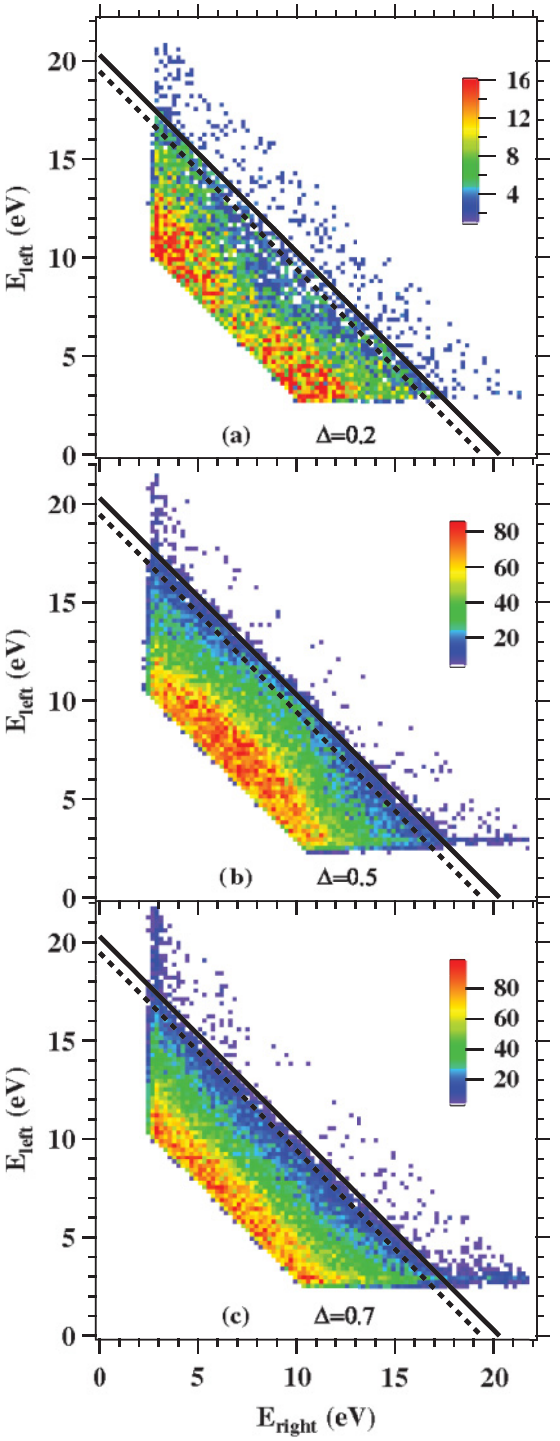


FIG. 7. (Color) Spin-integrated 2D-energy distributions for different values of Δ are shown. These were obtained with $E_p = 25$ eV. The solid diagonal line indicates the energetic position of the onset of pair emission. The dashed diagonal marks the $E_{\text{sum}}$ value if the valence electron stems from a level 0.8 eV below $E_F$.

given value of $E_{\text{sum}}$ the coincidence intensity is essentially constant. These 2D-energy distributions demonstrate that the geometrical constraint imposed has a strong impact. It is appropriate to have a closer look on these energy distributions. For this we compute so-called sharing curves. For this it is required to chose a value for $E_{\text{sum}}$. Coincidence events

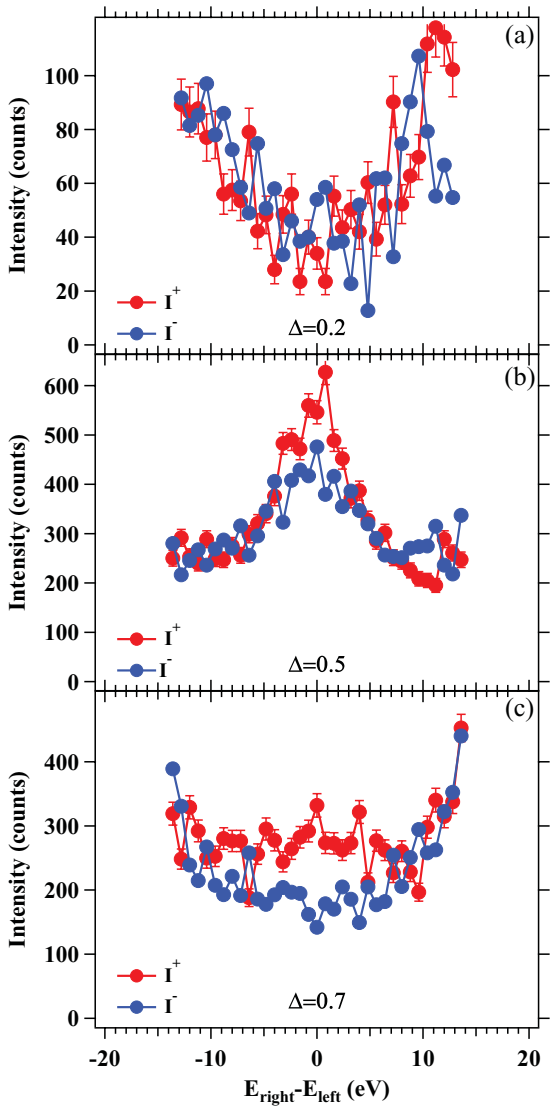


FIG. 8. (Color) From the 2D-energy distribution shown in Fig. 7 spin-resolved sharing curves are computed. The primary energy was set to $E_p = 25$ eV. The red (blue) symbols refer to parallel (antiparallel) alignment of the primary spin and majority.

for which $E_{\rm sum} = \text{const}$ are diagonal lines in the 2D-energy distributions; see Fig. 7. The intensity along such a line is plotted against the energy difference $E_r - E_l$. In the following we want to focus on those events where $E_{\rm sum} = E_{\rm sum}^{\rm max} - 0.8$ eV. In order to get spin-resolved sharing curves we consider the subsets $I^+$ and $I^-$ separately. Before we discuss this we would like to point out the following. Although a spectrum is defined from $-E_{\rm sum}$ to $E_{\rm sum}$ our instrument has a low kinetic-energy cutoff therefore we cannot measure the full sharing curve. In Fig. 8(a) we display the sharing curve for $\Delta = 0.2$. The spin contrast is essentially zero for the whole spectrum. It is apparent that the probability for both electrons to have the same energy is strongly reduced compared to unequal energies. If $\Delta = 0.5$ is selected the situation has changed significantly. First we see a clear preference for equal energies. Second, for equal energies there is a higher intensity for $I^+$ than for $I^-$. Increasing $\Delta$ to 0.7 we obtain strongly spin-dependent but relatively flat sharing functions with maxima at the outermost values of $E_r - E_l$.

## III. THEORY

While our experimental $(e,2e)$ spectra—for a given primary spin orientation—in general are a sum over contributions involving both spin-up and spin-down valence electrons (with energy and surface-parallel momentum determined by the respective conservation law), theory can obtain these contributions separately. This allows more detailed insight into exchange and Coulomb correlation effects. Calculating in addition the valence electronic structure, we can elucidate the relationship between spin-dependent $(e,2e)$ spectra and the spin-, momentum-, and symmetry-resolved valence electron density of states. The latter is furthermore useful for identifying energy and parallel-momentum conditions, for which valence electrons of one spin type and two spatial symmetry types predominate. As will be explained below, this makes it possible to separate exchange and Coulomb correlation effects directly in the experimental spectra.

In this section, we first outline the theoretical methods used for calculating the valence electron structure and $(e,2e)$ spectra, and then present and discuss prototype numerical results for ferromagnetic Fe(001).

### A. Theoretical formalism and model specifications

For the calculation of the electronic structure of the ground state we employed an *ab initio* full-potential linear augmented-plane-wave (FLAPW) method.[26] Using a local-density approximation for the exchange-correlation energy,[27] we applied this method to a ferromagnetic Fe(001) film consisting of 21 monoatomic layers, with the first interlayer spacing reduced by 5% relative to the bulk Fe interlayer spacing and the second interlayer spacing expanded by 5%, as had been determined by a low-energy electron diffraction (LEED) analysis.[28] We thereby obtained the spin-, layer-, and symmetry-resolved density of states (referred to in the following as LDOS), which is the key quantity for interpreting $(e,2e)$ spectra. Further, we calculated the spin-resolved charge density, which is needed for the construction of the quasiparticle potential input for our $(e,2e)$ calculations.

For the calculation of $(e,2e)$ reaction cross sections we used a formalism that has previously been presented in detail.[7] We therefore recall here only the key concepts and the most essential expressions. The central ingredients are transition-matrix elements between a two-quasiparticle initial state, which is an antisymmetrized product of the one-particle states describing primary and valence electron, and a two-quasiparticle final state, which involves the two outgoing electron states correlated by the screened Coulomb interaction. Due to the antisymmetrization there are two types of matrix elements: direct and exchange ones. In the absence of spin-orbit coupling, which is small for Fe and can be neglected in the present applications, the direct matrix elements reduce to the form

$$f^{\sigma\tau} = \langle l^\sigma r^\tau | U | p^\sigma \rangle | v^\tau \rangle, \tag{6}$$

where $|p^\sigma\rangle$ and $|v^\tau\rangle$ are the (spin-dependent) spatial parts of the primary and the valence electron states with spin orientations $\sigma = \pm$ and $\tau = \pm$ relative to the majority spin axis of the target. $U$ denotes the screened Coulomb interaction. The two detected electrons are described by an antisymmetric two-electron state, the direct spatial part of which is

$$|l^\sigma r^\tau\rangle = |l^\sigma\rangle|r^\tau\rangle F_{\rm corr}(\mathbf{k},\mathbf{r}), \tag{7}$$

where $|l^\sigma\rangle$ and $|r^\tau\rangle$ are the spatial parts of time-reversed LEED states. These are coupled by the Coulomb correlation factor $F_{\rm corr}(\mathbf{k},\mathbf{r})$, which is a function of the relative momentum $\mathbf{k}$ and the relative coordinate $\mathbf{r}$ obtained as the numerical solution of a relative-particle Schrödinger equation involving $U$.[7]

Because of the antisymmetry of the two-electron states we have, in addition to the direct matrix elements $f^{\sigma\tau}$ [cf. Eq. (6)], exchange matrix elements $g^{\sigma\tau}$, which are analogous to $f^{\sigma\tau}$, with $l^\sigma$ and $r^\tau$ interchanged.

For the cases of spin $\sigma$ of the primary electron parallel and antiparallel to the spin $\tau$ of the valence electron, i.e., $\tau = \sigma$ and $\tau = -\sigma = \bar{\sigma}$, we then have the fully spin-resolved $(e,2e)$ reaction cross sections,

$$I^{\sigma\sigma} \propto |f^{\sigma\sigma} - g^{\sigma\sigma}|^2\delta \;\text{ and }\; I^{\sigma\bar{\sigma}} \propto (|f^{\sigma\bar{\sigma}}|^2 + |g^{\sigma\bar{\sigma}}|^2)\delta, \tag{8}$$

where $\delta$ symbolizes the conservation of energy and surface-parallel momentum. Summation over the valence electron spins yields the experimentally observable intensities

$$I^+ = I^{++} + I^{+-} \;\text{ for primary electron spin up,} \tag{9a}$$
$$I^- = I^{-+} + I^{--} \;\text{ for primary electron spin down.} \tag{9b}$$

For the application of the above $(e,2e)$ formalism to Fe(001) we constructed from our ground-state spin densities spin-dependent effective quasiparticle potentials. These contain in particular spin-dependent imaginary self-energy parts $V_{\rm im}^\sigma$, with $\sigma = +$ for spin-up and $\sigma = -$ for spin-down electrons. For the valence electrons, we took

$$V_{\rm im}^\sigma(E) = a^\sigma \frac{|E - E_F|}{|E - E_F| + 10.0} - 0.025(\text{eV}), \tag{10}$$

where $E$ is the electron energy in eV and the constant coefficient $a^\sigma$ is $a^+ = -4.05$ for spin up and $a^- = -1.35$ for spin down. In the energy range between the Fermi energy and about 4 eV below, which is relevant in our $(e,2e)$ context, this simple form approximates reasonably well the numerical results obtained by a many-body (local-density approximation (LDA)–dynamical mean-field theory (DMFT)] calculation.[29] As an important feature, we note that the lifetime of majority spin holes is much shorter than that of minority spin holes.

For the primary electron and the two detected electrons, which are represented by LEED states, we assumed the imaginary self-energy part

$$V_{\rm im}^\sigma(E) = a^\sigma(E + b^\sigma)^{c^\sigma}, \tag{11}$$

where $E$ is the kinetic energy in eV, $V_{\rm im}^\sigma$ is in eV, and the constant coefficients are $a^+ = -0.22$, $b^+ = 2.67$, $c^+ = 0.69$, $a^- = -0.33$, $b^- = 4.67$, $c^- = 0.62$. By virtue of the relation

$$\lambda^\sigma = \sqrt{2(\tilde{E} + \tilde{V}_r)}/\left(2\tilde{V}_{\rm im}^\sigma\right), \tag{12}$$

where $\tilde{V}_r$ is the real part of the inner potential in Hartree atomic units and $\tilde{E}$ and $\tilde{V}_{\rm im}^\sigma$ are the respective quantities in Hartree. This choice is in quantitative accordance with experimental data for the spin-dependent mean-free path $\lambda^\sigma$, which shows that spin-down electrons are more strongly damped than spin-up electrons.[30–32] In terms of the bulk interlayer spacing of Fe(001) (2.71 bohr), some typical values of $\lambda^\sigma$ are the following. For primary electrons with kinetic energy 25 eV, $\lambda^+$ and $\lambda^-$ are 3.88 and 3.12, respectively. For the outgoing electron energy 10 eV, we have 5.18 and 3.77.

Using the above $V_{\rm im}^\sigma$ [Eq. (11)] in a spin-dependent LEED calculation from Fe(001), we obtained the best agreement with experimental data.[33] In our present $(e,2e)$ calculations, this $V_{\rm im}^\sigma$ yields significantly better agreement with our experimental data than a spin-independent $V_{\rm im}$.

The electron-electron interaction $U$ in Eq. (6) should strictly speaking be a Coulomb potential, which is screened in terms of a dielectric function $\epsilon(\mathbf{r},\mathbf{r}')$, which continuously decreases from the bulk screening deep inside the solid to the surface dielectric response and eventually to no screening in the vacuum region. In the absence of a first-principles knowledge of such a dielectric function and in view of tractability within our layer–Korringa-Kohn-Rostoker (KKR)-type formalism, we took the electron-electron interaction inside the solid in the Thomas-Fermi approximation $U \propto \exp(-q_{TF}r)/r$. The Thomas-Fermi wave number $q_{TF}$ was treated as a parameter, which we determined by comparing calculated $(e,2e)$ energy and momentum distributions with their experimental counterparts (see Sec. IV below). The Coulomb repulsion in the vacuum region is not included explicitly, but mimicked by a weakening of the effective screening in the topmost atomic layers. Since the emission of low-energy electron pairs originates mainly from the first two layers, as will be demonstrated below, the thus obtained effective Thomas-Fermi wave number $q_{TF} = 0.1\,\text{bohr}^{-1}$ (see Sec. IV below) accounts for the Coulomb interaction in the topmost layers and in the near-surface vacuum. Consequently it is much smaller than the bulk value $q_{TF} = 0.9\,\text{bohr}^{-1}$.

The correlation hole in our $(e,2e)$ momentum distributions is due to the Coulomb interaction after the collision. Its spatial origin is the following. In reality, it is made in a few near-surface atomic layers of the solid and in the near-surface vacuum region. In our formalism, with the above-discussed Thomas-Fermi screening, it originates in a few near-surface atomic layers, in which we adopt a weakening of the screening of the Coulomb interaction in order to mimic the repulsion in the near-surface vacuum region.

### B. Valence electron densities of states and $(e,2e)$ spectra for Fe(001)

As the most pertinent result of our *ab initio* FLAPW calculation of the electronic structure of Fe(001) we show in Fig. 9 the spin-, $\vec{k}^{\parallel}$-, and layer-resolved valence electron density of states (LDOS) $N_m^\tau(E,k_x)$ [with $k_x$ along the $\overline{\Gamma}(\Delta)\overline{H}$ direction in the surface Brillouin zone], with $\tau = \pm$ indicating majority/minority spin and $m = 1,2$, bulk referring to the topmost, second, and bulk layers parallel to the surface. Since the contour plots are rather self-explanatory, it may suffice to point out a few salient features. Just around the Fermi

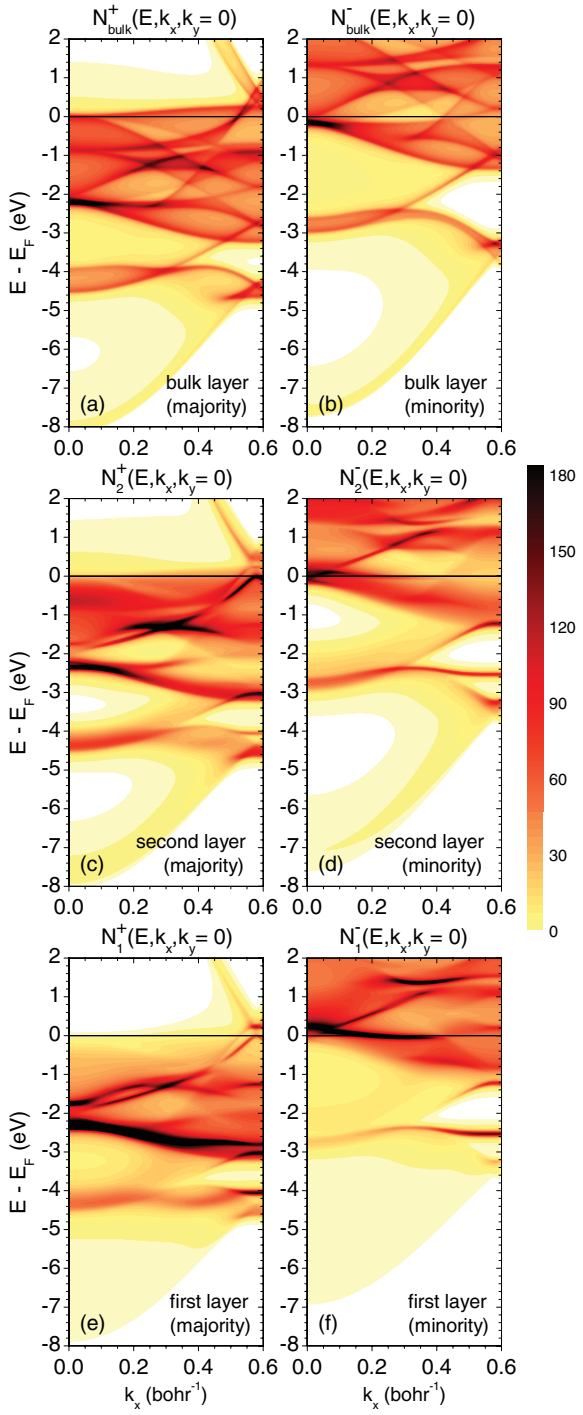


FIG. 9. (Color) $\mathbf{k}^{\|}$- and layer-resolved valence electron density of states (LDOS) $N_m^\tau(E,k_x)$ [with $k_x$ along the $\overline{\Gamma}(\Delta)\overline{H}$ direction in the surface brillouin zone]. To reveal more details, the imaginary potential part has been chosen as a very small constant ($-0.05$ eV). (a),(b) Bulk layer majority and minority spin LDOS, respectively; (c),(d) second layer majority and minority spin LDOS, respectively; (e),(f) first layer majority and minority spin LDOS, respectively.

energy, there is a clear dominance of minority spin over majority spin, in accordance with earlier *ab initio* calculation results. In particular, there are two strong minority surface-state/resonance bands, as can be seen in panel (f) in comparison with panel (b). These results are in accordance with earlier *ab initio* calculations.[34,35]

Digressing briefly to the $\mathbf{k}^{\|}$-integrated LDOS $N_m^\tau$, we note that at $E_F$ minority spin exceeds majority spin in the surface layer (ratio $N_1{}^- : N_1{}^+ = 9.40$), whereas in the bulk it is the other way around ($N_1{}^- : N_1{}^+ = 0.24$). This agrees well with the results of earlier calculations.[34] Also in line with earlier work[34,36] is an enhancement of the magnetic moment at the surface by 30% with respect to the bulk magnetic moment.

Further below $E_F$, Fig. 9 reveals that there is mainly majority spin with pronounced second-layer and bulk LDOS features for small $k_x$ between about $-0.5$ and $-1.0$ eV. As is seen in panel (e), in comparison to panel (a), there is a small majority-spin surface resonance band at $E = -1.8$ eV for small $k_x$ and a very strong majority surface resonance band dispersing downward from $E = -2.2$ eV over the entire surface Brillouin zone.

In view of analyzing $(e,2e)$ spectra with the aid of selection rules (cf. Refs. 6 and 37) we show in Figs. 10 and 11 the LDOS of Fe(001) at the $\overline{\Gamma}$ point ($k_x = 0$) resolved not only with respect to spin and layers, but also with respect to the spatial symmetry types $\Delta_1, \Delta_{2'}, \Delta_2, \Delta_5$. In order to display individual LDOS features and their relation to the bulk band structure more clearly, we show in Fig. 10 results that have been computed with a very small constant imaginary potential part ($V_{\rm im} = 0.05$ eV) instead of the much larger energy-dependent $V_{\rm im}^\sigma$ [cf. Eq. (10)]. For both majority and minority spin, the bulk layer LDOS curves are seen to correspond in the usual way to the respective bulk band structure along $\Gamma(\Delta)H$. A prominent highly localized minority spin surface state of $\Delta_1$ symmetry is seen at 0.234 eV above $E_F$, in line with the results of earlier calculations and of scanning tunneling experiments (cf. Refs. 35 and 38, and references therein). Turning to the states below $E_F$, which are relevant for $(e,2e)$, we would like to emphasize the following. In a very close vicinity of $E_F$, minority spin states of $\Delta_5$ symmetry strongly dominate. At energies below about $-0.4$ eV majority spin states of all symmetry types have sizable weight, whereas minority spin states appear only for $\Delta_2$ with small weight over a wider range and for $\Delta_1$ as a narrow peak around $-2.8$ eV. As can be seen in Fig. 11, these characteristics persist in the quasiparticle LDOS calculated with the realistic larger $V_{\rm im}^\sigma$ according to Eq. (10).

We now address the relationship between quasiparticle LDOS and observable $(e,2e)$ spectra. First, we would like to explore how the LDOS $N_m^\tau(E,k_x)$ manifests itself in $(e,2e)$ energy distributions $I(E_r,E_\ell)$, where $E_r$ and $E_\ell$ are the energies of the two outgoing electrons. To this end, it is convenient to plot the LDOS as a function of $E_r$ and $E_\ell$. This is possible, since—by virtue of energy and parallel momentum conservation (cf. above Sec. II)—fixed energies and surface-parallel momenta of the primary and the outgoing electrons are uniquely related to energy and parallel momentum of the valence electron.

Since the LDOS near the surface differs from layer to layer, an adequate quantity for comparing with $(e,2e)$ energy distributions $I^{\sigma\tau}$ is a weighted sum $N^{\sigma\tau}$ over the near-surface layer densities of states $N_m^\tau$, with weight factors $w_m^{\sigma\tau}$

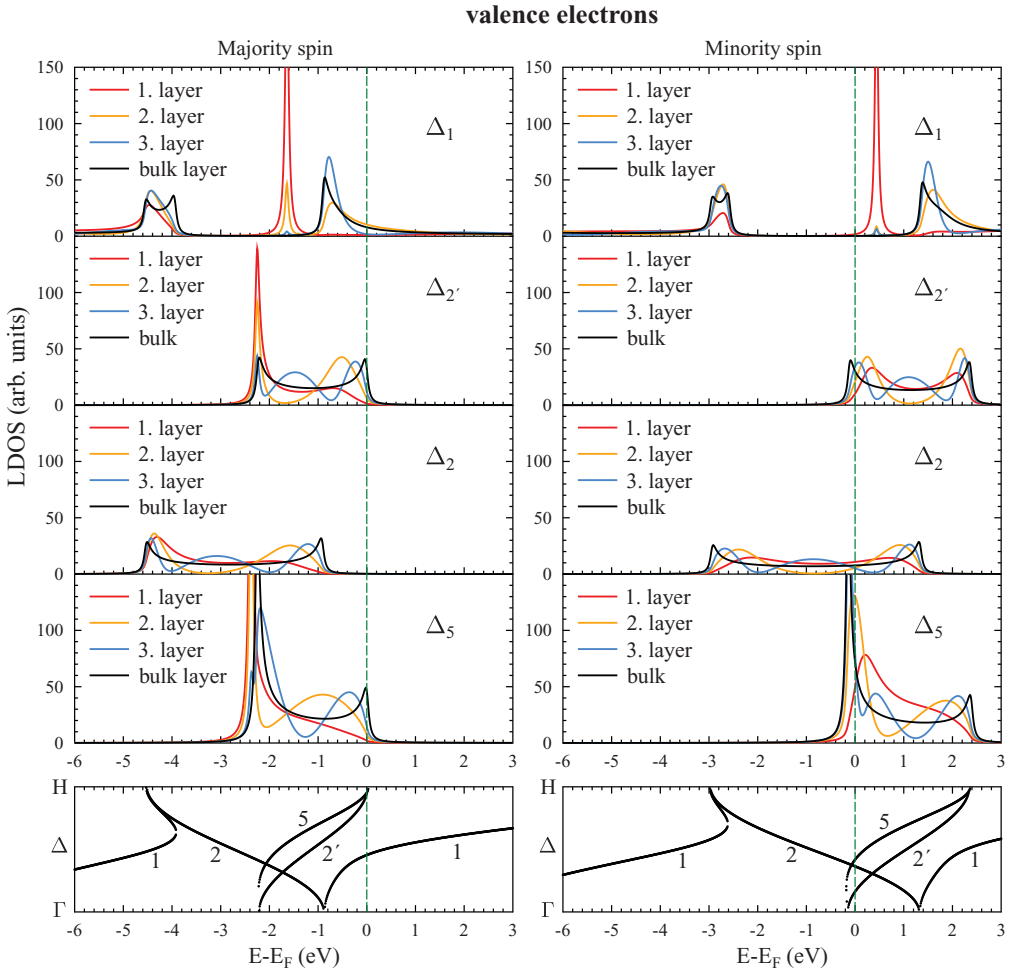


FIG. 10. (Color) Valence electron states of Fe(001) for $\mathbf{k}^{\parallel} = 0$. Bottom panels: majority and minority spin bulk band structure along $\Gamma(\Delta)H$ with the symbols 1, 2, 2′, and 5 indicating the spatial symmetry types $\Delta_1, \Delta_{2'}, \Delta_2, \Delta_5$ of the individual bands. Upper panels: spin- and layer-resolved densities of states (LDOS) of first (red lines), second (yellow lines), third (blue lines), and bulk (black lines) Fe layers for the individual $\Delta$ symmetry types as indicated in the panels. For clearer graphical presentation, a small constant imaginary part ($V_{\rm im} = -0.05$ eV) has been added to the (real) ground-state potential in the LDOS calculation.

determined by the spin-dependent mean free path $\lambda^{\pm}$ [cf. Eq.(12)] of the primary and the outgoing electrons:

$$N^{\sigma\tau} = \sum_m w_m^{\sigma\tau} N_m^{\tau} \tag{13}$$

$$\text{with} \quad w_m^{\sigma\tau} := \exp\left[-d_m\left(\frac{1}{\lambda_1^{\sigma}} + \frac{1}{\lambda_2^{\sigma}} + \frac{1}{\lambda_2^{\tau}}\right)\right];$$

$\sigma$ indicates the spin of the primary electron and of one of the outgoing ones, $\tau$ is the spin of the other outgoing electron; $m$ counts the layers parallel to the surface, $d_m$ is the distance between the nominal surface plane and the internuclear plane of the $m$th layer; $\lambda_1^{\sigma}$ is the mean free path of the primary electron, and $\lambda_2^{\sigma}$ and $\lambda_2^{\tau}$ are the mean free paths of the two outgoing electrons.

In Fig. 12 we demonstrate the relation between the LDOS sum $N^{\sigma\tau}$ [cf. Eq. (13)] and $(e,2e)$ energy distributions $I^{\sigma\tau}(E_r, E_\ell)$ for the case of a normally incident primary electron with energy 25 eV and coplanar emission of the two electrons at equal polar angles 30°. The reaction plane is chosen as the $(x,z)$ plane, which is a mirror plane of the semi-infinite crystal. Consequently, only valence electron states of even symmetry with respect to this plane are allowed to contribute to the $(e,2e)$ intensity, as has been derived in previous work.[37] We therefore have to restrict the LDOS sum $N^{\sigma\tau}$ to even states.

With the primary energy fixed (25 eV), the spin-dependent layer weight coefficients $w_m^{\sigma\tau}$ in Eq. (13) still depend on the energies of the emitted electrons. This dependence turned out, however, to be rather weak for the emitted electron energies under consideration. It therefore suffices to discuss the weight coefficients obtained for the case that both energies are equal to 10 eV. For both primary and valence electron spin up, we have $w_1^{++} = 0.74$, $w_2^{++} = 0.40$, and $w_3^{++} = 0.20$ for the first, second, and third layer, respectively. For both spins down, the corresponding values are $w_1^{--} = 0.67$, $w_2^{--} = 0.30$, and $w_3^{--} = 0.12$. In the two opposite-spin cases we have $w_m^{+-} > w_m^{-+}$ with values in between those of $w_m^{++}$ and $w_m^{--}$. Comparing the coefficients with each other we first note a pronounced spin dependence, which increases from the first to the third layer. Second, the coefficients for a given spin configuration decrease rapidly from layer to layer, implying that $(e,2e)$ is strongly surface sensitive.

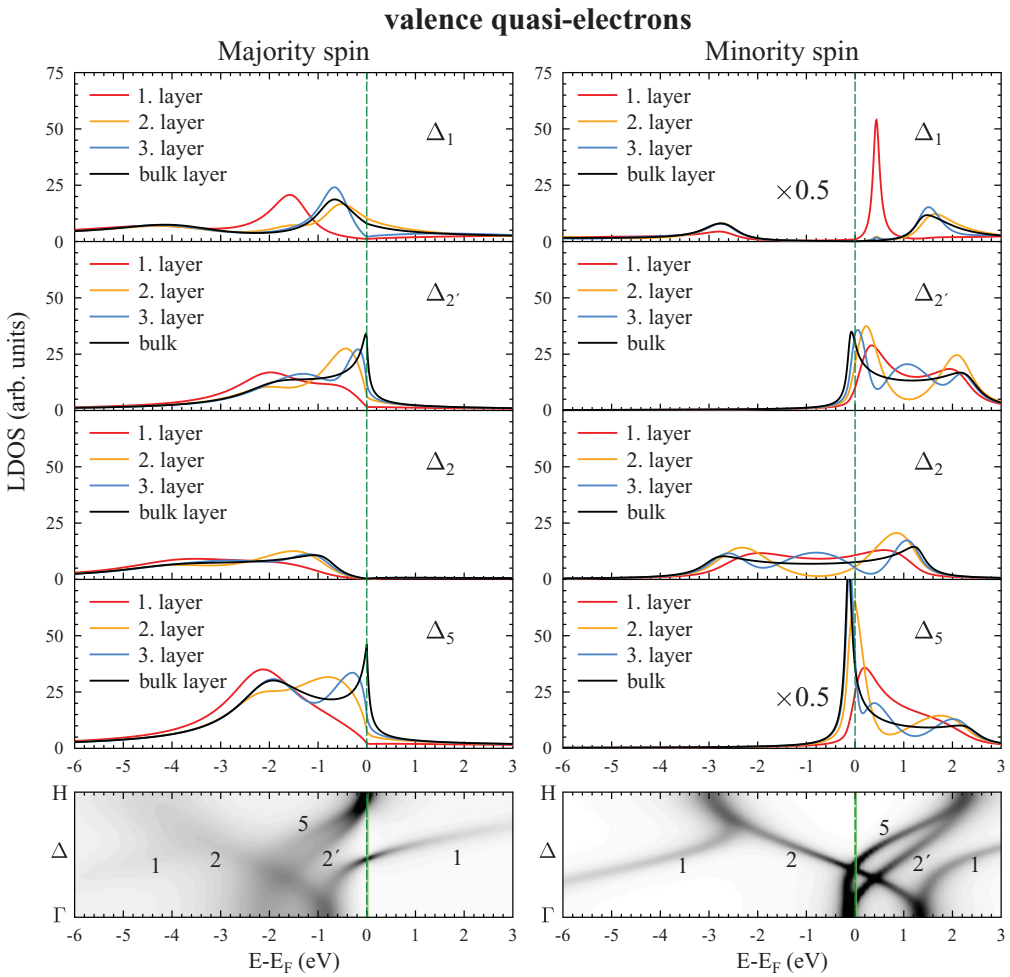


FIG. 11. (Color) Valence quasi-electrons of Fe(001) for $\mathbf{k}^{\parallel} = 0$, which are excited in the $(e,2e)$ process. The individual panels are analogous to those in Fig. 10, but both bulk bands and LDOS have been calculated using the spin- and energy-dependent imaginary part $V_{\mathrm{im}}^{\sigma}(E)$ of Eq. (10).

Turning now to the relation between LDOS sums and $(e,2e)$ energy distributions, we first address the case of valence electron spin up. Comparing, for primary spin up, the LDOS sum $N^{++}$ in Fig. 12(a) with the parallel-spin intensity $I^{++}$ in Fig. 12(c), one first notices that for nearly equal energies of the two emitted electrons, corresponding to valence electron momentum $k^{\parallel}$ between $-0.1$ and 0.1, and valence energy between about 0.5 and 2 eV below $E_F$, $N^{++}$ is sizable and $I^{++}$ is very strong. For very different energies of the emitted electrons, corresponding to $|k^{\parallel}| > 0.2$, $N^{++}$ is of similar magnitude as in the central region, but $I^{++}$ is much weaker. Valence electron LDOS is thus seen to be a prerequisite for $(e,2e)$, but the actual size of the intensity depends on the four electron states entering in the $(e,2e)$ matrix elements [cf. Eq. (6)]. While the primary electron state is constant, the valence electron state and the outgoing electron states vary from point to point in the $(e,2e)$ energy distribution. For primary spin down, comparison of Figs. 12(b) and 12(d) shows that the antiparallel-spin intensity $I^{-+}$ is weak for $|k^{\parallel}| > 0.2$. In the central region ($|k^{\parallel}| < 0.1$), $I^{-+}$ is appreciable, but significantly smaller than the parallel-spin intensity $I^{++}$. For valence electron spin down, analogous results are shown in Figs. 12(e)–12(h). In particular, we note that for $|k^{\parallel}| < 0.1$ the antiparallel-spin intensity $I^{+-}$ rather closely reflects the LDOS, whereas $I^{--}$ is extremely small below $E_{\mathrm{valence}} = -2$ eV despite a large LDOS in this region.

These features are, for $|k^{\parallel}| = 0$, seen more quantitatively in Figs. 13(a)–13(d) in line scans across the diagonals of the individual panels of Fig. 12. Panels (a) and (c), which relate to majority-spin valence electrons, show that—despite very similar underlying weighted LDOS—$I^{++}$ has a single large peak centered around $-1.2$ eV, whereas $I^{-+}$ exhibits two maxima, which are much smaller. As a sufficient reason for a substantial difference between the two curves we point out that, by virtue of $(e,2e)$ selection rules for 4-mm symmetry surfaces and the present reaction plane (cf. upper half of Table I in Ref. 6), $I^{++}$ involves exclusively majority-spin valence electrons of spatial symmetry $\Delta_5$, whereas $I^{-+}$ can contain contributions from $\Delta_1$, $\Delta_2$, and $\Delta_5$ majority-spin valence electrons. The majority-spin LDOS curves (shown in Fig. 11) are in fact sizable for $\Delta_1$ and $\Delta_5$, and still appreciable for $\Delta_2$.

Comparing the intensity curves in panel (c), which were calculated for polar emission angles $\vartheta_r = \vartheta_\ell = 30^\circ$, with their analogs for 45° [panel (e)] we note substantial differences in size and shape. Since the underlying valence electron states are the same in the two cases, these differences must be due

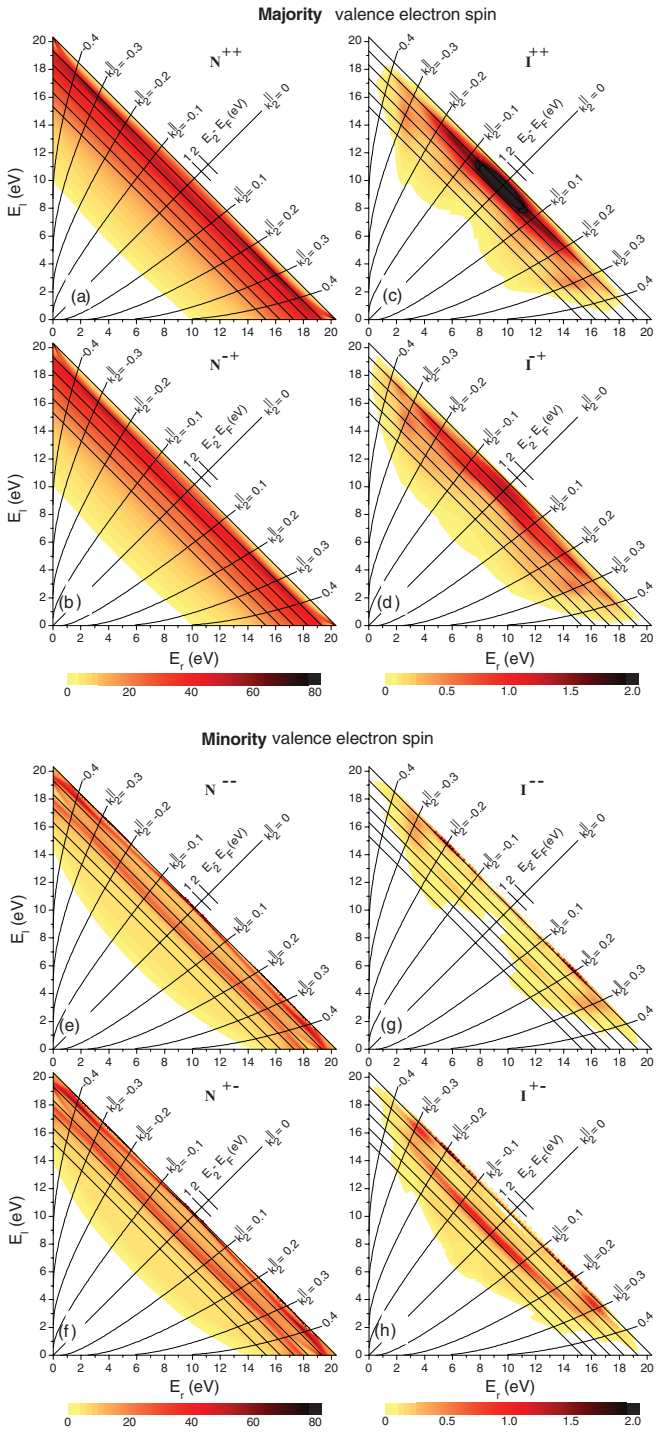


FIG. 12. (Color) Valence electron density of states and $(e,2e)$ energy distributions from Fe(001) for normally incident primary electron with energy 25 eV and outgoing electrons in the $(x,z)$ plane with equal polar angles $\vartheta_r = \vartheta_\ell = 30^\circ$ and azimuthal angles $\varphi_r = 0$ and $\varphi_\ell = 180^\circ$. Upper half [(a)–(d)], for spin-up (majority) valence electrons: (a) Weighted sum $N^{++}$ [cf. Eq. (13)] of the spin-up densities of even states $N_m^+(E,k_x)$ of the topmost three monoatomic layers parallel to the surface, which were calculated with the spin- and energy-dependent quasiparticle imaginary self-energy part $V_{\rm im}^\sigma(E)$ as in Eq. (10). In each panel, the diagonal axis represents the valence electron energy $E$ with respect to the Fermi energy. The axis normal to it is associated with the parallel momentum $k_x =: k_2^\parallel$ of the valence electron as indicated by the iso-$k_2^\parallel$ lines (in bohr$^{-1}$). (b) Weighted sum $N^{-+}$ [cf. Eq. (13)]. (c) Fully spin-resolved $(e,2e)$ energy distribution $I^{++}(E_r,E_\ell)$ [cf. Eq. (8)] for primary electron spin up. (d) $I^{-+}(E_r,E_\ell)$ for primary electron spin down. In the $(e,2e)$ calculations we employed the Thomas-Fermi wave number $q_{TF} = 0.1$ bohr$^{-1}$ in the screened Coulomb interaction, which we determined by comparisons with our experimental data (see Figs. 17 and 18, and associated text), and the spin-dependent imaginary self-energy parts given by Eqs. (10) and (11), with the latter corresponding to a spin-dependent mean free path for the primary and the outgoing electrons. Lower half [(e)–(h)], for spin-down (minority) valence electrons: (e),(f) Weighted LDOS sums $N^{--}$ and $N^{+-}$. (g),(h) $(e,2e)$ energy distributions $I^{--}(E_r,E_\ell)$ and $I^{+-}(E_r,E_\ell)$ for primary electron spin down and up, respectively.

to the different outgoing electron states in the $(e,2e)$ matrix elements. For minority valence electron spin, our findings are analogous and consistent with the symmetry-resolved minority LDOS curves (shown in Fig. 11), as can be seen in Figs. 13(b), 13(d), and 13(e).

From Fig. 13 it is obvious that the experimentally observable intensities $I^+$ and $I^-$ [i.e., $I^{\pm\tau}$ summed over the valence spin $\tau$, cf. Eq. (9)] both arise almost exclusively from collisions with majority-spin valence electrons, except at energies very close to the Fermi energy and, for $\vartheta = 30^\circ$, around $-2.8$ eV. This is in contrast to $(e,2e)$ results from Fe(110),[22,37] which show that—for equal energies of the two emitted electrons—$I^+$ ($I^-$) is for most energies associated with minority (majority) valence electrons, i.e., there is mostly singlet scattering between the primary and the valence electron. The reason for this difference between Fe(001) and Fe(110) is that valence states, which are odd with respect to reflection at a plane perpendicular to the scattering plane and thence lead to triplet scattering, occur for Fe(110) only in a very small energy range well below $E_F$, whereas for Fe(001) they are present over a wide energy range (cf. the $\Delta_5$ majority spin LDOS curves in Fig. 11).

Energy distributions—like the ones shown in Fig. 12—necessarily involve valence electron states with a range of energies and of parallel momenta. In contrast, parallel-momentum distributions (cf. Sec. II) for opposite momenta of the two outgoing electrons ($\mathbf{k_r} = -\mathbf{k}_\ell$) are associated with valence electrons of parallel momentum zero and fixed energy. Choosing—by virtue of energy conservation in $(e,2e)$—this energy such that valence electrons of one spin orientation strongly dominate in the LDOS and that this domination persists in the $(e,2e)$ spectra, one practically has an internal resolution of the valence electron spin over the entire parallel-momentum distribution.

We first select primary electron energy and outgoing electron energies such that the valence electron energy is $E_F$, where minority spin dominates (cf. Fig. 11). In Fig. 14 we show fully spin-resolved $(e,2e)$ momentum distributions $I^{\sigma\tau}(k_x,k_y)$ [cf. Eq. (8)] from Fe(001) in the surface-parallel momentum plane $(k_x,k_y)/k$. As an obvious consequence of the dominance of minority valence electron spin, we note that $I^{++}$ and $I^{-+}$, which involve majority valence spin, are overall much weaker than $I^{--}$ and $I^{+-}$, which involve minority valence spin.

The most important conclusion is reached by comparing, for given valence electron spin, the momentum distributions

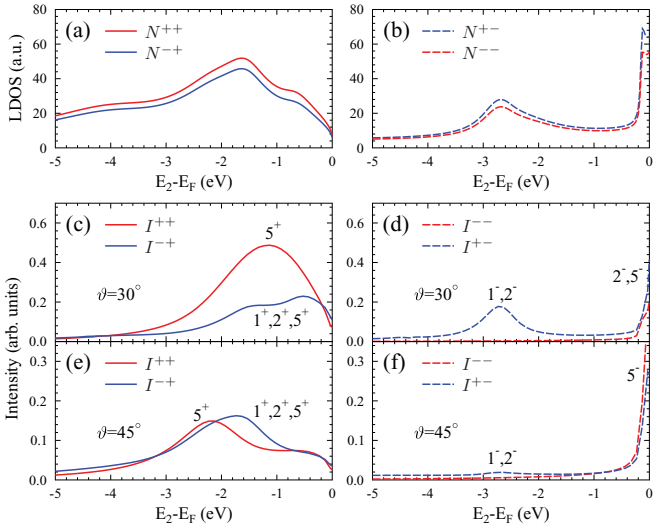


FIG. 13. (Color) For the same $(e,2e)$ setup as in Fig. 12 we show the weighted valence electron LDOS and $(e,2e)$ spectra for equal energies $E_r = E_\ell$, which are line scans along the diagonals of the panels of Fig. 12. The parallel momentum of the valence electron is thus always zero. Its energy relative to the Fermi energy is $E - E_F = 25 - 2E_r - \Phi$ (eV), and the $(e,2e)$ spectra $I^{\sigma\tau}$ can therefore also be plotted as functions of $E - E_F$. (a) Weighted sums $N^{++}$ (red line) and $N^{-+}$ (blue line) [cf. Eq. (13)] for majority-spin valence electrons. (b) Weighted sums $N^{+-}$ (blue line) and $N^{--}$ (red line) for minority-spin valence electrons. (c) $(e,2e)$ intensities $I^{++}$ (red line) and $I^{-+}$ (blue line) for polar angle $\vartheta = 30°$, associated with majority-spin valence electrons, i.e., line scans through Figs. 12(c) and 12(d). (d) $(e,2e)$ intensities $I^{+-}$ (red line) and $I^{--}$ (blue line) for polar angle $\vartheta = 30°$, associated with minority-spin valence electrons, i.e., line scans through Figs. 12(g) and 12(h). (e),(f) As (c) and (d), respectively, but for polar angle $\vartheta = 45°$ instead of 30°. The labels $1^\sigma$, $2^\sigma$, and $5^\sigma$ next to the intensity curves indicate the symmetry types $\Delta_1$, $\Delta_2$, and $\Delta_5$ and the spin ($\sigma = \pm$) of the valence electrons, from which contributions to the respective intensity are allowed by $(e,2e)$ selection rules (cf. upper half of Table I in Ref. 6). $\Delta_{2'}$ valence electrons cannot contribute at all, since their wave functions are antisymmetric with respect to the present $(e,2e)$ reaction plane.

for parallel spins with those for antiparallel spins. Going outward from the center to about $|\mathbf{k}^{||}|/k = 0.5$, all distributions exhibit a region of small intensity. This depletion zone is seen to be much more pronounced for parallel spins than for antiparallel ones. Since outgoing electrons with parallel spins are subject to exchange and Coulomb interaction, whereas those with antiparallel spins are correlated only by the Coulomb interaction, the central depletion zones in $I^{+-}$ and $I^{-+}$ can be viewed as a Coulomb correlation hole and those in $I^{++}$ and $I^{--}$ as an exchange plus Coulomb correlation hole. Our momentum distributions thus imply that the latter hole is larger than the former.

Summation over the valence electron spin yields the experimentally accessible intensities $I^+$ for primary spin up [Fig. 14(e)] and $I^-$ for primary spin down [Fig. 14(f)]. Due to the dominance of spin-down valence electrons at $E_F$, $I^+$ pertains essentially to antiparallel spins and $I^-$ to parallel spins.

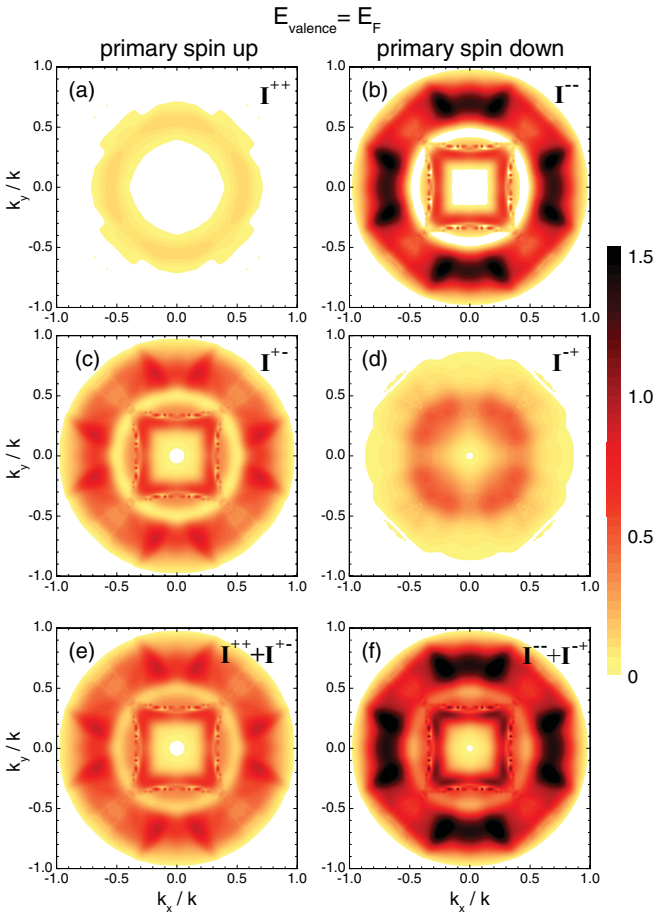


FIG. 14. (Color) Fully spin-resolved $(e,2e)$ momentum distributions $I^{\sigma\tau}(k_x,k_y)$ [cf. Eq. (8)] from Fe(001) in the surface-parallel momentum plane $(k_x,k_y)/k$, with $\sigma = \pm$ and $\tau = \pm$ labeling the spin of the primary and of the valence electron, respectively. In an equal energy sharing coplanar symmetric setup, primary electrons with energy 25 eV are normally incident. The two electrons are emitted at polar angle $\vartheta$ and azimuthal angles $\varphi$ and $\varphi + \pi$. They have equal energy $E = 10.165$ eV and surface-parallel momenta $(k_x,k_y) = \sqrt{2E}\sin\vartheta(\cos\varphi, \sin\varphi)$ and $(-k_x, -k_y)$. Taking into account the work function value 4.67 eV, the relevant valence electron thus has parallel momentum 0, energy 0 relative to the Fermi energy, and majority/minority spin $\tau = \pm$. In the calculations we employed the Thomas-Fermi wave number $q_{TF} = 0.1$ bohr$^{-1}$ in the screened Coulomb interaction, which we determined by comparisons with our experimental data (see Figs. 17 and 18, and associated text), and the spin-dependent imaginary self-energy parts given by Eqs. (10) and (11). In (a) and (b) the spins are parallel, i.e., the two electrons are correlated by exchange and by Coulomb interaction. In the antiparallel spin case in (c) and (d), there is only Coulomb correlation between the two electrons. Panel (e) shows, for a spin-up primary electron, the sum over the contributions from spin-up and spin-down valence electrons, i.e., the sum over (a) and (c). Panel (f) is the analog for primary spin down.

In Fig. 15 we present fully spin-resolved $(e,2e)$ momentum distributions $I^{\sigma\tau}(k_x,k_y)$ [cf. Eq. (8)] with primary and outgoing electron energies such that the valence electron energy is 0.8 eV below $E_F$, where majority spin strongly dominates. These results are in essence analogous to those in Fig. 14, with "spin up" and "spin down" interchanged. In particular, we find

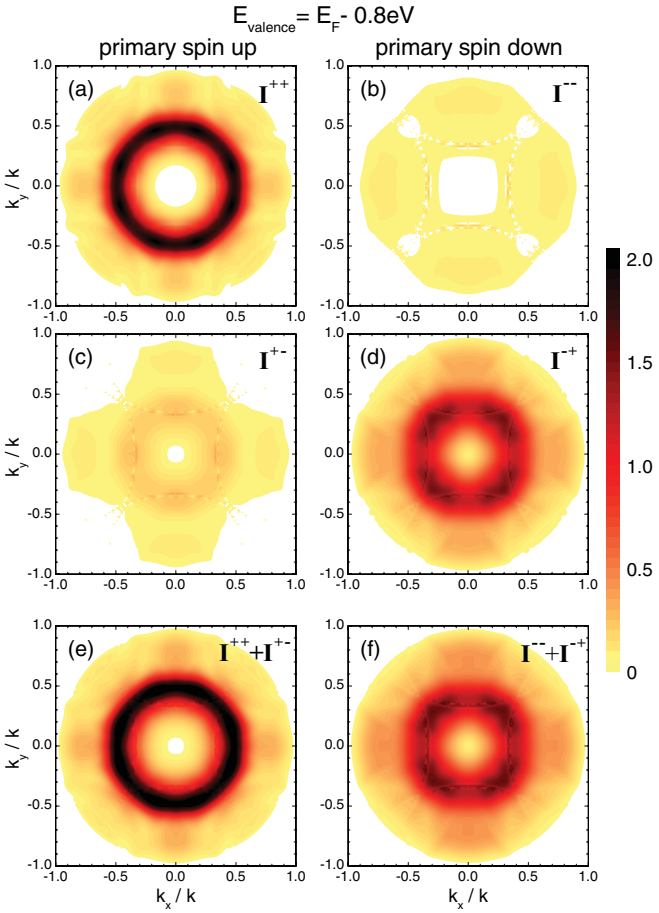


FIG. 15. (Color) As in Fig. 14 except that the energy of each of the two emitted electrons has been chosen as 9.765 eV, which implies that the energy of the relevant valence electron is −0.8 eV with respect to the Fermi level, where there is a strong dominance of majority spin.

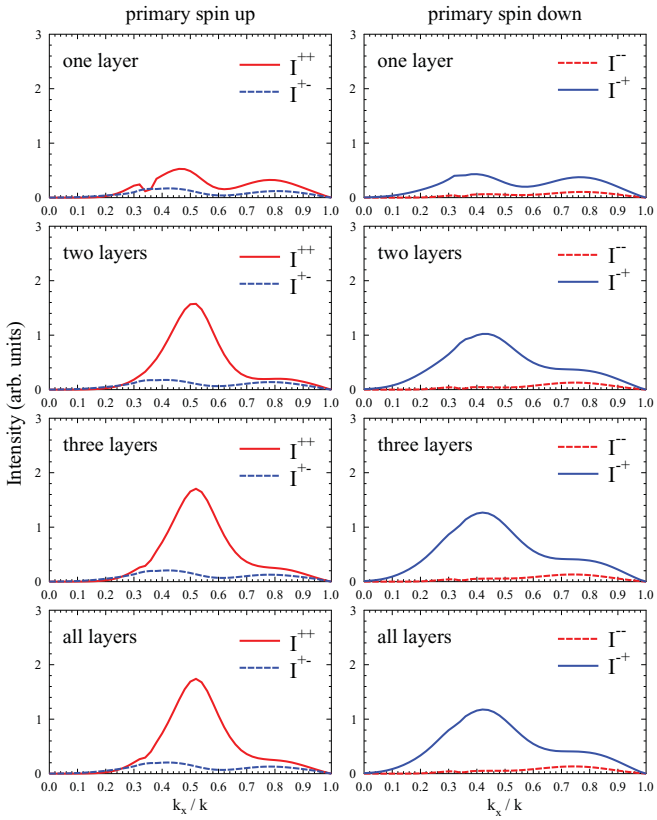


FIG. 16. (Color) Fully spin-resolved $(e,2e)$ intensities $I^{\sigma\tau}(k_x,k_y=0)$ [cf. Eq. (8)] from Fe(001) for valence electron energy −0.8 eV. The bottom panels are line scans along the $k_x$ axis through the corresponding angular distributions $I^{\sigma\tau}(k_x,k_y)$ shown in Fig. 15. While they were obtained in calculations for the complete Fe(001) half space, i.e., for all monoatomic layers parallel to the surface, corresponding intensities, which arise from the first $N=1,2,3$ layers, are shown in the upper panels (with $N$ indicated in the respective panels).

that the exchange plus Coulomb correlation hole exhibited by $I^{++}$ [panel (a)] and in good approximation by $I^{+}$ [panel (e)] is larger than the Coulomb correlation hole in $I^{-+}$ [panel (d)] and $I^{-}$ [panel (f)].

A more quantitative view of the fully spin-resolved momentum distributions associated with dominant majority spin valence electrons at −0.8 eV is provided in the bottom panels of Fig. 16 by line scans $I^{\sigma\tau}(k_x,k_y=0)$ along the $k_x$ axis through the corresponding angular distributions $I^{\sigma\tau}(k_x,k_y)$ shown in Fig. 15. The line scans in the bottom panels result from calculations for the complete Fe(001) half space, i.e., comprising all monoatomic layers parallel to the surface.

The very high surface sensitivity of $(e,2e)$ from Fe(001), which follows from the mean-free-path-derived weight coefficients $w_m^{\sigma\tau}$ [cf. Eq. (13) and subsequent text], is demonstrated in a more quantitative and detailed way by the upper panels of Fig. 16. In these we show $(e,2e)$ intensities, which arise from only the first $N$ surface-parallel monoatomic layers of the semi-infinite crystal, with $N=1,2,3$ in the first, second, and third row of panels, respectively.

For primary spin up (left-hand column of panels of Fig. 16) we first note that the dominant $I^{++}$ peak from two layers is more than twice the size of its counterpart from just the first layer. This appears plausible from the $(e,2e)$ selection rules (cf. Table I in Ref. 6), according to which parallel-spin intensities arise only from valence electron states of $\Delta_5$ spatial symmetry, and from the observation (in Fig. 11) that at valence energy −0.8 eV the $\Delta_5$ LDOS in the second layer is about twice as high as in the first layer. One may therefore wonder why the second maximum of the first layer $I^{++}$, which is associated with the very same valence electron state, gets reduced when two layers contribute. The puzzle of the different behavior of the two maxima is resolved by recognizing that the intensity from two layers is not a sum of the intensities from the individual layers but rather the absolute square of the sum of the amplitudes (matrix elements), which allows both constructive and destructive interference. Since the two-electron final state is quite different for the two maxima, so are the matrix elements. A high LDOS in a given layer is thus a necessary but by no means sufficient condition for a substantial intensity increase upon including this layer.

For primary spin down, the two maxima in the first layer $I^{-+}$ are seen to change similarly when going to two layers.

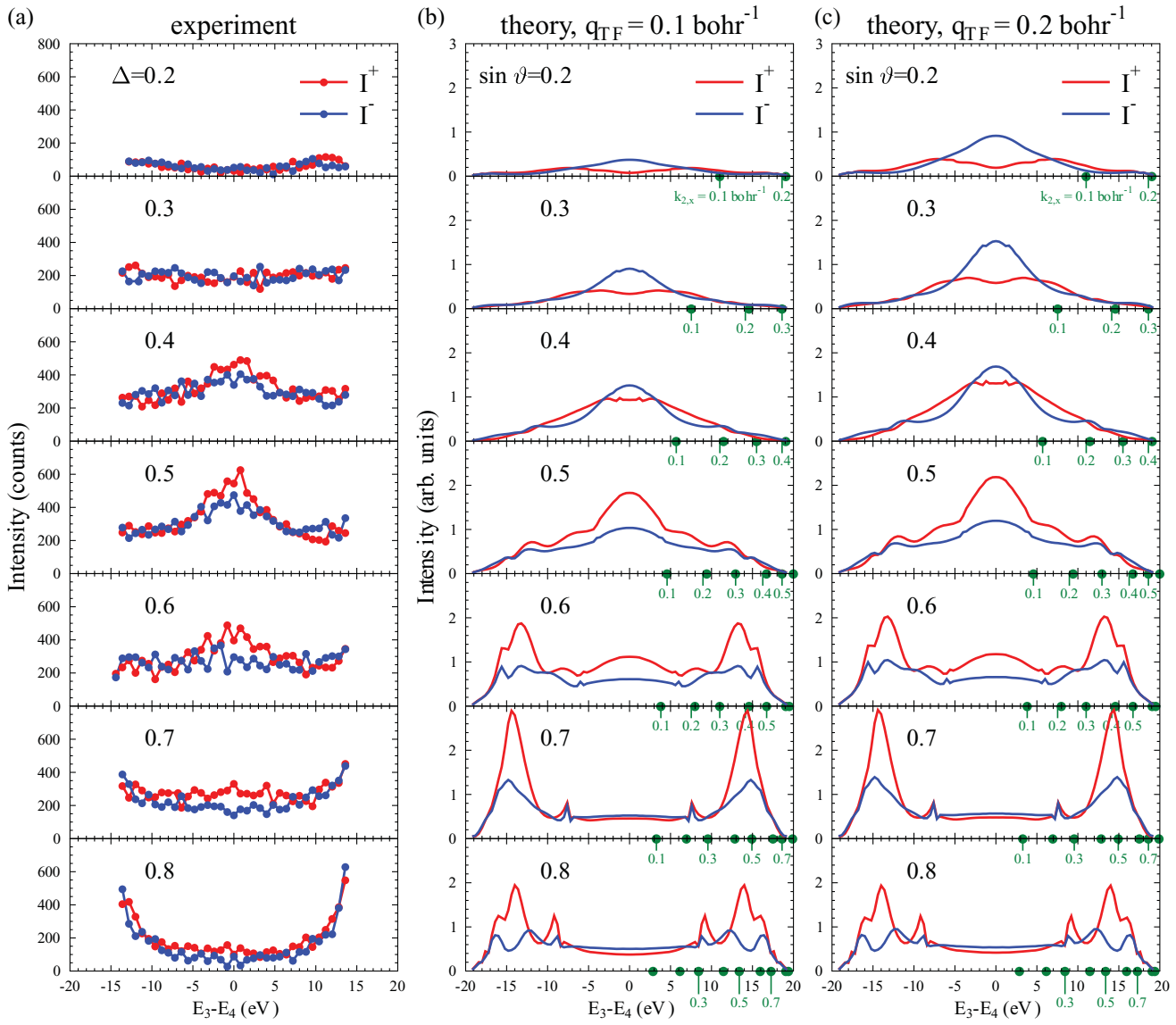


FIG. 17. (Color) $(e,2e)$ energy sharing curves $I^{\pm}(E_r - E_\ell)$ from Fe(001) for primary electrons with energy 25 eV and spin $\sigma = \pm$ and for constant sum energy $E_r + E_\ell = 19.53$ eV of the two outgoing electrons. By virtue of energy conservation, the valence electron energy thence is fixed as $E_F - 0.8$ eV. In all panels, the red (blue) curves represent $I^+$ ($I^-$) obtained for primary electron spin up (down). Left-hand column of panels: Experimental sharing curves, which were obtained from the experimental raw data as described in Sec. II C in the context of Fig. 6. Events with polar emission angles $\vartheta_r$ and $\vartheta_\ell$ are included subject to the restriction that the normalized parallel momenta (with absolute values $\sin\vartheta_r$ and $\sin\vartheta_\ell$) are between the two circles with mean radius $\Delta$ (cf. Fig. 6). Central column of panels: Theoretical sharing curves for Coulomb screening parameter $q_{TF} = 0.1$ bohr$^{-1}$. All curves are for constant polar emission angles $\vartheta_r = \vartheta_\ell =: \vartheta$, with the value of $\sin\vartheta$ indicated in the individual panels. For equal energy sharing, i.e., $E_r = E_\ell$, the valence electron has parallel momentum 0. For unequal energies $E_r \neq E_\ell$, selected values of $E_r - E_\ell$ are marked by fat green dots on the energy axis and the associated parallel momentum of the valence electron is indicated (in bohr$^{-1}$ units) by the green numbers next to each dot. The arbitrary intensity units are the same for all panels. Note that for $E_r = E_\ell$ the intensity values are the same as those at the respective $k_x/k = \sin\vartheta$ in the momentum distribution line scans (when summed over the valence electron spins), which are shown in the bottom panel of Fig. 16. Right-hand column of panels: Theoretical sharing curves as in central column, but for screening parameter $q_{TF} = 0.2$ bohr$^{-1}$.

According to $(e,2e)$ selection rules, (majority) valence electron states of spatial symmetry $\Delta_1$, $\Delta_2$, and $\Delta_5$ are allowed to contribute. The LDOS in Fig. 11 shows that the former two types are, like the latter one, stronger in the second layer than in the first one. Therefore the behavior of the two $I^{-+}$ maxima can be interpreted in the same way as above for $I^{++}$.

As can be seen in Fig. 16, the spectra from two layers are already very close to the complete ones, and those from three layers are practically the same.

### IV. COMPARISON OF EXPERIMENT AND THEORY

In this section we present and discuss experimental $(e,2e)$ energy sharing and momentum distributions from Fe(001) together with their theoretical counterparts. Energy distributions like the experimental spin-integrated one $I(E_r,E_\ell)$ in Fig. 7 and the theoretical spin-resolved ones $I^{\pm}(E_r,E_\ell)$ in Fig. 12 cover, for fixed emission angles, the whole range of the sum energy $E_{\rm sum} = E_r + E_\ell$ and thereby of the valence electron energy, which is allowed by energy conservation. As was shown in Sec. II (see Fig. 8 and associated text), more details are, however, revealed by so-called energy sharing curves, which are, for fixed $E_{\rm sum}$ and thence fixed $E_{\rm valence}$, diagonal line scans across the corresponding energy distributions.

In Fig. 17 we show spin-dependent energy sharing curves $I^{\pm}(E_r - E_\ell)$ from Fe(001) for a wide range of constant polar emission angles $\vartheta_r = \vartheta_\ell =: \vartheta$. The primary electron being 25 eV, we chose $E_{\rm sum} = 19.53$ eV. By virtue of energy conservation, the valence electron energy is then $E_F - 0.8$ eV, where there is a strong dominance of majority spin for small values of the surface-parallel momentum.

Experimental energy sharing curves are shown in the left-hand column of Fig. 17. For $\sin\vartheta = 0.2$, the spin contrast is essentially zero over the whole spectrum, and the probability for both electrons to have the same energy is reduced compared to unequal energies. Going to $\sin\vartheta = 0.5$, we observe significant changes. First, there is a clear preference for equal energies. Second, the $I^+$ peak is higher than the $I^-$ peak. Proceeding to larger values of $\sin\vartheta$, the sharing curves become very small and almost constant except for a rise close to the maximum energy difference, which we can detect.

In the central and in the right-hand column of Fig. 17 we show corresponding theoretical energy sharing curves $I^{\pm}(E_r - E_\ell)$. In the calculations we included the Coulomb correlation between the two outgoing electrons—via the correlation factor $F_{\rm corr}(\mathbf{k},\mathbf{r})$ [cf. Eq. (7)]—and used the spin-dependent imaginary self-energy parts [see Eqs. (10) and (11)]. As for the screened Coulomb interaction in the Thomas-Fermi approximation, we regard the Thomas-Fermi wave number $q_{TF}$, which characterizes the screening strength, as a parameter to be determined by comparison with our experimental spectra. It suffices to show energy sharing curves for the values $q_{TF} = 0.1$ bohr$^{-1}$ and 0.2 bohr$^{-1}$, since significantly smaller and larger values can be excluded on the grounds of momentum distributions (see below Fig. 18 and its context).

In both theoretical sets we notice mostly the same features as above in the experimental set. For $\sin\vartheta = 0.5$, there is a pronounced spin-dependent maximum at equal energies, which turns into a minimum for larger angles. Going to smaller angles, $I^+$ has again a minimum, whereas for $I^-$ there is some discrepancy between experiment and theory: the calculated $I^-$ has a maximum at equal energies, which is, however, much smaller for $q_{TF} = 0.1$ bohr$^{-1}$ than for $q_{TF} = 0.2$ bohr$^{-1}$. Since $I^-$ pertains to antiparallel spins of the outgoing electrons, the size of this maximum is inversely related to the size of the correlation hole. Comparison of the two theoretical sets with experiment favors $q_{TF} = 0.1$ bohr$^{-1}$. For $q_{TF} > 0.2$ bohr$^{-1}$ (stronger screening), the $I^-$ peak at equal energies for $\sin\vartheta = 0.2$ increases further. Significantly smaller $q_{TF}$ values can be ruled out by comparing calculated momentum distributions with their experimental counterparts, as will be demonstrated later on.

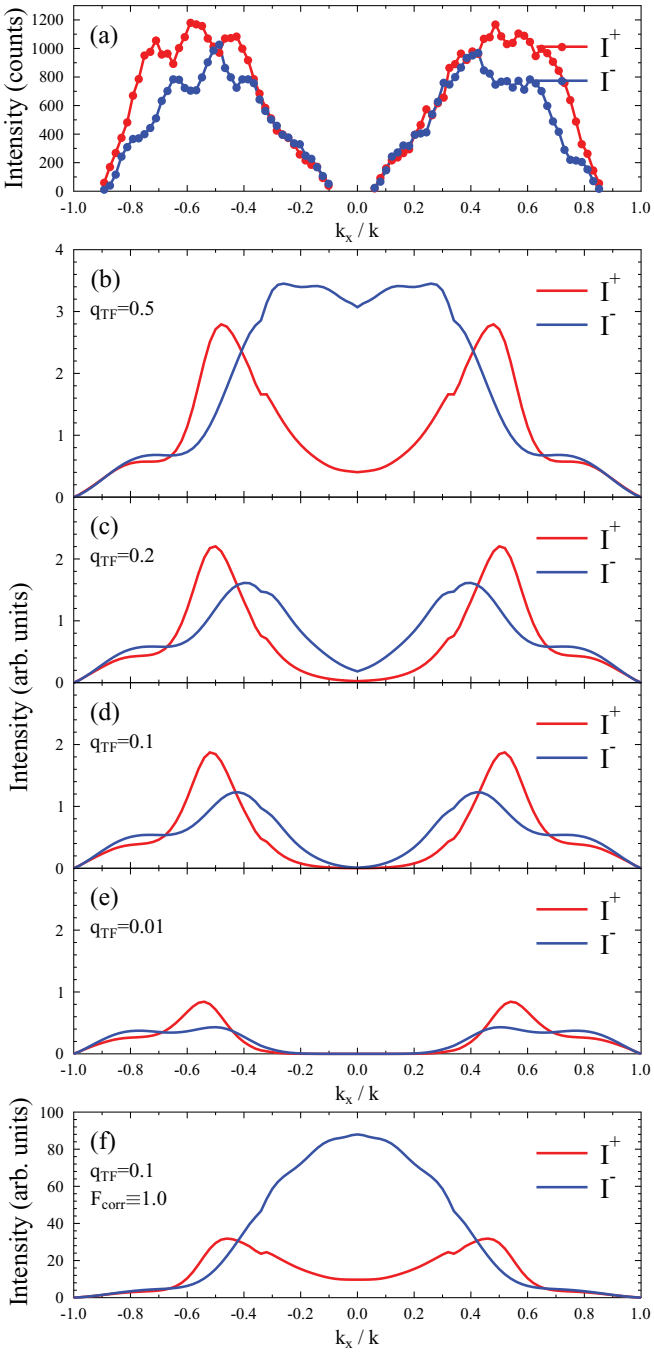


FIG. 18. (Color) Spin-dependent momentum distribution line scans $I^{\sigma}(k_x,k_y = 0)$ for $\varphi = 0$ for primary electron energy 25 eV, valence electron with energy $E_F - 0.8$ eV, and surface-parallel momentum 0. (a) Experiment; (b)–(e) theory [cf. Eq. (9)], with Coulomb correlation between the two outgoing electrons [via numerically calculated $F_{\rm corr}(\mathbf{k},\mathbf{r})$ in Eq. (7)] for a range of Thomas-Fermi screening parameter $q_{TF}$ values (in bohr$^{-1}$) as indicated in the panels; (f) without Coulomb correlation [by setting $F_{\rm corr}(\mathbf{k},\mathbf{r}) \equiv 1$] for screening parameter $q_{TF} = 0.1$ bohr$^{-1}$.

But first we would like to draw attention to two further features of the theoretical sharing curves at larger angles. All curves in the $\sin\vartheta = 0.6$ panels exhibit a fine structure around $|E_r - E_\ell| = 6$ eV, which increases and moves toward larger $|E_r - E_\ell|$ with increasing $\sin\vartheta$. This feature originates from a surface resonance in the lower-energy outgoing LEED state, which is associated with an emergence threshold of nonspecular beams.

The big peaks at large energy differences, which dominate the theoretical spectra for $\sin\vartheta \geqslant 0.6$, are seen (from the green $k_x$ values in the plots) to involve valence electrons with $k_x > 0.3$. As is evident from the LDOS plots $N_m^\tau$ in Fig. 9, at the chosen energy $-0.8$ eV minority spin has similar weight as majority spin for these larger $k_x$. Consequently, $I^+$ ($I^-$) is no longer approximately equal to $I^{++}$ ($I^{-+}$), as is the case for small $k_x$, but contains a sizable contribution $I^{+-}$ ($I^{--}$).

In Fig. 18 we show spin-dependent momentum distribution line scans $I^\pm(k_x, k_y = 0)$ for $\varphi = 0$, i.e., emission in the $(x,z)$ plane. We recall from above that the associated valence electron parallel momentum is zero. By virtue of energy conservation, the valence electron energy was chosen as $-0.8$ eV ($\pm 0.2$ eV experimentally), where majority spin strongly dominates over minority spin. As one would therefore expect and as has been explicitly shown in Fig. 16, $I^+$ ($I^-$) consists mainly of $I^{++}$ ($I^{-+}$), i.e., is associated with parallel (antiparallel) spins of the two detected electrons.

The experimental spectra [in Fig. 18(a)] exhibit the following main features. There is a central depletion zone, i.e., reduced intensity for small momenta, which is due to exchange and Coulomb correlation. Going toward larger momentum values (corresponding to larger polar emission angles) all curves reach maxima, with the $I^+$ peaks being further out and exceeding the $I^-$ peaks.

In Figs. 18(b)–18(e) we show corresponding theoretical momentum distributions. In all these calculations we included the Coulomb correlation between the two outgoing electrons via the correlation factor $F_{\rm corr}(\mathbf{k},\mathbf{r})$ [cf. Eq. (7)]. The sensitivity of the calculated momentum distributions to the assumed value of the Thomas-Fermi parameter $q_{TF}$ is demonstrated by comparing with each other Figs. 18(b)–18(e), which were obtained for $q_{TF}$ as indicated in the panels. The most striking effect is seen to occur in $I^-$, which pertains to antiparallel spins of the two outgoing electrons, at very small momentum values. For $q_{TF} = 0.01$ bohr$^{-1}$ [Fig. 18(e)], there is a very extended depletion zone (correlation hole), which decreases with increasing $q_{TF}$ (stronger screening). For $q_{TF} = 0.5$ bohr$^{-1}$ [Fig. 18(b)] it is already almost absent. For larger $q_{TF}$, the central intensity gets even larger and one has a central accumulation zone (correlation hill) instead of a correlation hole. This correlation trend also affects $I^+$ (parallel spins), where it is, however, overshadowed by exchange, which causes a central depletion zone also for larger $q_{TF}$.

Comparing with our experimental momentum distributions in Fig. 18(a), we note the following. For the large $q_{TF}$ values (strong screening), the correlation hole in $I^-$, which appears in the experimental spectra, is absent. For very small $q_{TF}$ [like 0.01 bohr$^{-1}$ in panel (d)], the correlation hole in $I^-$ as well as the exchange-correlation hole in $I^+$ are too extended. For $q_{TF} = 0.1$ bohr$^{-1}$ and $q_{TF} = 0.2$ bohr$^{-1}$, the overall agreement with experiment is of equally good quality. Since the energy sharing curves in Fig. 17 have been found to discriminate between these two values in favor of $q_{TF} = 0.1$ bohr$^{-1}$, we consider the latter as the optimal one.

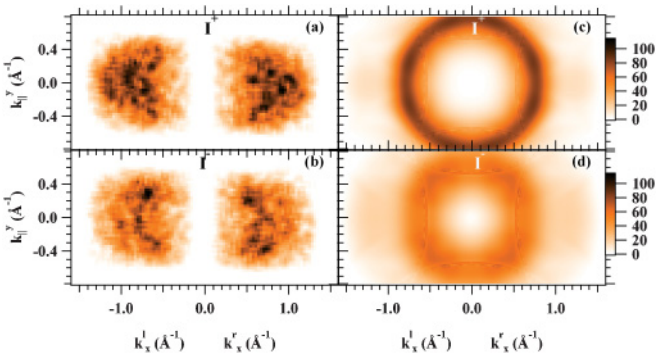


FIG. 19. (Color) Spin-dependent momentum distributions $I^+(k_x,k_y)$ and $I^-(k_x,k_y)$ for primary electron energy 25 eV and valence electron with energy $E_F - 0.8$ eV and surface-parallel momentum 0. (a),(b) Experiment; (c),(d): theory [cf. Eq. (9)], with screening parameter $q_{TF} = 0.1$ bohr$^{-1}$ and Coulomb correlation [via $F_{\rm corr}(\mathbf{k},\mathbf{r})$ in Eq. (7)].

If the Coulomb correlation between the two detected electrons is neglected—by taking the Coulomb correlation factor $F_{\rm corr} \equiv 1$ instead of the function $F_{\rm corr}(\mathbf{k},\mathbf{r})$ [cf. Eq. (7)]—the $I^-$ curve, which pertains to antiparallel spins of the two outgoing electrons, is affected most strikingly [see Fig. 18(f)]. Instead of the correlation hole in the curve in Fig. 18(d), there is a very pronounced maximum, which is in strong contradiction to our experimental data. From analogous calculations for different values of the screening parameter $q_{TF}$ we find that this maximum even increases for larger $q_{TF}$ and does not disappear for smaller ones.

To highlight the most important result of the present work, we complement the line scans shown in Fig. 18 by juxtaposing in Fig. 19 experimental spin-dependent momentum distributions $I^\sigma(k_x,k_y)$ and their theoretical counterparts (replotted from the bottom panels of Fig. 15 within the $\mathbf{k}^{||}$ window, which is accessible experimentally). Exchange and Coulomb correlation produce a central depletion zone in the parallel-spin distribution $I^+$, which is more extended than its counterpart in the antiparallel-spin distribution $I^-$, which is due to Coulomb correlation only.

## V. CONCLUDING REMARKS

The screening of the Coulomb interaction in the surface and near-surface region is strictly speaking represented by a very complicated dielectric function. In the absence of a first-principles knowledge for the Fe(001) surface and in order to be able to handle it within our layer-KKR-based $(e,2e)$ formalism, we have approximated it by a simple Thomas-Fermi form with an effective screening strength $q_{TF}$, which we regarded as a parameter to be determined by comparing experimental $(e,2e)$ spectra for antiparallel spins and small emission angles with their calculated counterparts. We thus found the value $q_{TF} = 0.1$ bohr$^{-1}$.

From a spin-dependent mean free path model for the primary and the outgoing electrons, which is based on earlier experimental data, we found that only the first three monoatomic layers should contribute significantly to the observable $(e,2e)$ spectra. This high surface sensitivity was quantitatively corroborated by comparing momentum distributions, which were calculated for one, two, and three layers, with the distributions obtained for the semi-infinite crystal.

Comparison of valence electron layer densities of states (LDOS), which we obtained by an *ab initio* FLAPW calculation, with $(e,2e)$ energy distributions demonstrates that a sizable underlying LDOS of the appropriate spatial symmetry type is a necessary but by no means sufficient condition for sizeable $(e,2e)$ features to occur. Matrix element effects, in particular interference of amplitudes arising from different layers, may in fact lead to a very small $(e,2e)$ intensity associated with regions of high LDOS.

From our spin-, $k_{||}$-, symmetry-, and layer-resolved LDOS we identified valence electron energy and parallel-momentum conditions, for which first one spin orientation dominates and second valence states exist of even and of odd symmetry with respect to a mirror plane perpendicular to the reaction plane. These two symmetries ensure, for equal energy sharing and emission in a mirror plane, that pair emission can occur for both primary spin orientations. For primary electrons with spin parallel to this dominant spin orientation of the valence electrons, $(e,2e)$ spectra are subject to exchange and Coulomb correlation, whereas for primary electrons with opposite spin, i.e., antiparallel spins of the two electrons, there is only Coulomb correlation. In both cases, momentum distributions were found to exhibit a central depletion zone ("hole"), which is, however, significantly larger for parallel than for antiparallel spins. The exchange-correlation hole in momentum space is thus larger than the correlation hole.


[1] J. Ullrich, R. Moshammer, A. Dorn, R. Dörner, L. Ph. H. Schmidt, and H. Schmidt-Böcking, Rep. Prog. Phys. **66**, 1463 (2003).

[2] L. Avaldi and A. Huetz, J. Phys. B **38**, S861 (2005).

[3] A. Knapp, A. Kheifets, I. Bray, Th. Weber, A. L. Landers, S. Schössler, T. Jahnke, J. Nickles, S. Kammer, O. Jagutzki, L. Ph. H. Schmidt, M. Schöffler, T. Osipov, M. H. Prior, H. Schmidt-Böcking, C. L. Cocke, and R. Dörner, J. Phys. B **38**, 615 (2005).

[4] R. Feder and H. Gollisch, in *Solid State Photoemission and Related Methods*, edited by W. Schattke and M. A. Van Hove (Wiley-VCH, Weinheim, 2003), Chap. 9.

[5] F. O. Schumann, J. Kirschner, and J. Berakdar, Phys. Rev. Lett. **95**, 117601 (2005).

[6] U. Rücker, H. Gollisch, and R. Feder, Phys. Rev. B **72**, 214424 (2005).

[7] H. Gollisch, N. V. Schwartzenberg, and R. Feder, Phys. Rev. B **74**, 075407 (2006).

[8] F. O. Schumann, C. Winkler, and J. Kirschner, New J. Phys. **9**, 372 (2007).

[9] B. D. Napitu, Y. Pavlyukh, and J. Berakdar, J. Phys. Conf. Ser. **141**, 012010 (2008).

[10] M. Munoz-Navia, C. Winkler, R. Patel, M. Birke, F. O. Schumann, and J. Kirschner, J. Phys.: Condens. Matter **21**, 35503 (2009).

[11] F. O. Schumann, C. Winkler, J. Kirschner, F. Giebels, H. Gollisch, and R. Feder, Phys. Rev. Lett. **104**, 087602 (2010).

[12] N. Fominykh, J. Berakdar, J. Henk, S. Samarin, A. Morozov, F. U. Hillebrecht, J. Kirschner, and P. Bruno, in *Solid State Photoemission and Related Methods*, edited by W. Schattke and M. A. Van Hove (Wiley-VCH, Weinheim, 2003), Chap. 10.

[13] M. Hattass, T. Jahnke, S. Schössler, A. Czasch, M. Schöffler, L. Ph. H. Schmidt, B. Ulrich, O. Jagutzki, F. O. Schumann, C. Winkler, J. Kirschner, R. Dörner, and H. Schmidt-Böcking, Phys. Rev. B **77**, 165432 (2008).

[14] F. O. Schumann, C. Winkler, and J. Kirschner, Phys. Status Solidi B **246**, 1483 (2009).

[15] E. Wigner and F. Seitz, Phys. Rev. **43**, 804 (1933).

[16] J. C. Slater, Rev. Mod. Phys. **6**, 209 (1934).

[17] *Density Functional Theory*, edited by E. K. U. Gross and R. M. Dreizler, NATO ASI Series B337 (Plenum Press, New York, 1995).

[18] W. Kohn, Rev. Mod. Phys. **71**, 1253 (1999).

[19] E. Engel and R. M. Dreizler, *Density Functional Theory* (Springer, Heidelberg, Dordrecht, London, New York, 2011).

[20] J. Berakdar, H. Gollisch, and R. Feder, Solid State Commun. **112**, 587 (1999).

[21] S. N. Samarin, J. Berakdar, O. Artamonov, and J. Kirschner, Phys. Rev. Lett. **85**, 1746 (2000).

[22] A. Morozov, J. Berakdar, S. N. Samarin, F. U. Hillebrecht, and J. Kirschner, Phys. Rev. B **65**, 104425 (2002).

[23] D. T. Pierce and F. Meier, Phys. Rev. B **13**, 5484 (1976).

[24] N. Fominykh, J. Berakdar, J. Henk, and P. Bruno, Phys. Rev. Lett. **89**, 086402 (2002).

[25] F. O. Schumann, C. Winkler, and J. Kirschner, Phys. Rev. Lett. **98**, 257604 (2007).

[26] See [www.flapw.de].

[27] S. H. Vosko, L. Wilk, and M. Nusair, Can. J. Phys. **58**, 1200 (1980).

[28] Z. Q. Wang, Y. S. Li, F. Jona, and P. M. Marcus, Solid State Commun. **61**, 623 (1987).

[29] L. Chioncel, L. Vitos, I. A. Abrikosov, J. Kollár, M. I. Katsnelson, and A. I. Lichtenstein, Phys. Rev. B **67**, 235106 (2003).

[30] D. P. Pappas, K. P. Kämper, B. P. Miller, H. Hopster, D. E. Fowler, C. R. Brundle, A. C. Luntz, and Z. X. Shen, Phys. Rev. Lett. **66**, 504 (1991).

[31] M. Getzlaff, J. Bansmann, and G. Schönhense, Solid State Commun. **87**, 467 (1993).

[32] F. Passek, M. Donath, and K. Ertl, J. Magn. Magn. Mater. **159**, 103 (1996).

[33] R. Bertacco and F. Ciccacci, Phys. Rev. B **59**, 4207 (1999).

[34] S. Ohnishi, A. J. Freeman, and M. Weinert, Phys. Rev. B **28**, 6741 (1983).

[35] J. A. Stroscio, D. T. Pierce, A. Davies, R. J. Celotta, and M. Weinert, Phys. Rev. Lett. **75**, 2960 (1995).

[36] M. Eder, K. Terakura, and J. Hafner, Phys. Rev. B **64**, 115426 (2001).

[37] H. Gollisch and R. Feder, J. Phys.: Condens. Matter **16**, 2207 (2004).

[38] M. M. J. Bischoff, T. K. Yamada, C. M. Fang, R. A. de Groot, and H. van Kempen, Phys. Rev. B **68**, 045422 (2003).